

Facile Synthesis of SnS Nanostructures With Different Morphologies for Supercapcitor and Dye-Sensitized Solar Cell Applications

Mohd Arif Dar (✉ dararifphy@gmail.com)

Annamalai University <https://orcid.org/0000-0001-9569-0224>

D. Govindarajan

Annamalai University

Gulam Nabi Dar

University of Kashmir

Research Article

Keywords: XRD, UV- V spectroscopy, FTIR, DSSC, Specific capacitance.

Posted Date: March 19th, 2021

DOI: <https://doi.org/10.21203/rs.3.rs-289278/v1>

License:  This work is licensed under a Creative Commons Attribution 4.0 International License.

[Read Full License](#)

Version of Record: A version of this preprint was published at Journal of Materials Science: Materials in Electronics on July 15th, 2021. See the published version at <https://doi.org/10.1007/s10854-021-06550-w>.

Facile synthesis of SnS nanostructures with different Morphologies for Supercapcitor and dye-sensitized solar cell Applications

Mohd Arif Dar¹, D. Govindarajan¹, Gulam Nabi Dar²,

¹*Department of Physics, Annamalai University, Annamalai Nagar, India*

²*Department of physics, university of Kashmir, Srinagar, Jammu and Kashmir, India.*

Email: dararifphy@gmail.com

Abstract

In this paper, Tin Sulfide (SnS) nanoparticles is synthesized with three different solvents through hydrothermal method and characterized by using X-Ray diffraction, scanning electron microscopy, UV–Drs spectroscopy, Fourier transform infrared spectroscopy, Energy Dispersive X- ray spectrum, Supercapcitor and photovoltaic performance. XRD patterns indicate that the prepared SnS nanoparticles exist in the orthorhombic phase. The SEM analysis clearly picturize the morphological changes in the SnS nanoparticles synthesized through different solvents. The UV-Drs spectrum gives direct energy band gap which lies between 1.0 eV to 2.0 eV. The FT-IR spectrum explains various functional groups present in the SnS nanoparticles. The prepared SnS counter electrodes (CEs) showed good electrocatalytic activity in the redox reaction of the I^-/I_3^- . The efficiency of SnS-e, SnS-a and SnS-m counter electrodes are 9.99 %, 9.90 % and 9.86 % in Dye-sensitized solar cells (DSSC) than that of platinum counter electrode which is 9.80 %. The specific capacitance of 284 F/g is obtained for SnS-e electrode at a current density of 5 A/g and an energy density of 216 Wh/kg corresponding to power density value of 1.6 KWh/kg which proves SnS-e electrode possesses better capacitive performance.

Keywords: XRD; UV- V spectroscopy; FTIR; DSSC; Specific capacitance.

Corresponding author*: dararifphy@gmail.com

Introduction

In recent years, nanostructured semiconductors have attracted greater interest due to their significant applications in electronic, optical and superconductor devices [1–3]. The key properties of these nanostructured materials rely upon their designs including morphology, geometry and hierarchical structures [4]. Currently, scientist much effort has been made to develop novel techniques to synthesize nanostructured metal chalcogenide semiconductors such as GeSe, GeS, SnS, SnSe, PbSe and PbS due to their various potential applications like infrared sensors, photo transducers, optical and photovoltaic properties etc. [5–7]. Among these chalcogenide semiconductors, SnS have got greater research interest because of its layered structure, narrow band gap, high absorption coefficient in the visible region, chemical stability, carrier mobility and p-type electrical conductivity [8]. This layered structure in tin sulfides effectively promote the intercalation of ions (Na⁺ and Li⁺) during electrochemical reactions and makes them more favourable and alternative anodic material for supercapacitor applications [9]. SnS nanomaterial with different morphology also plays key role in photocatalytic properties, electrical and optical features for use in solar cells. Presently, researchers put more efforts for the preparation of SnS nanostructures with different morphologies like nanorods, nanoflowers, dendrite-like nanoparticles, nanosheets, belt-like nanocrystals through hydro/solvothermal methods [11-15].

In this study, SnS nanospheres are synthesized by simple, surfactant free solvothermal method using ethanol, methanol and acetone as a solvent. The final product was characterized using XRD, FT-IR, UV-DRS, SEM and EDX techniques. The prepared SnS electrodes are examined for photovoltaic and electrochemical performance.

1. Experimental Procedure

1.1 Materials and methods

The chemicals used for the synthesis of SnS nanoparticles are tin (II) chloride (SnCl₂·2H₂O, Sigma-Aldrich 98% purity), Thioacetamide (Sigma-Aldrich 99 % purity) and Acetic acid (HPLC company Ltd. India, 99.7 % purity). All other solvents used were purchased from Loba chemical limited, india.

For synthesization, 0.1 mmol of SnCl₂·2H₂O was dissolved in 5 ml of acetic acid with constant stirring at room temperature. After 5 minutes, 50 ml of ethanol plus 0.75 g of TAA is added to the solution. After all the precursors are dissolved and a homogenous solution is formed, then the solution was transferred to a Teflon-lined stainless

steel autoclave and heated in an electric oven at 200 °C for 24 hrs. The obtained yellow colour precipitates were washed with distilled water several times so that all the impurities are removed and dried in a hot electric oven for 10 hrs at 60 °C temperature. Finally, the obtained product was ground with the help of agate mortar and pestles and named as SnS-e. The same procedure is repeated for other solvents such as methanol and acetone and the final product is named as SnS-m, SnS-a, respectively.

1.2 Synthesis of SnS hybrid CEs

The obtained yellow colour SnS material was dispersed in hexamethylene with a concentration of 0.08 g ml⁻¹ to form SnS hybrid ink. Three different SnS-e, SnS-m and SnS-a hybrid CEs were fabricated by directly drop-casting the ink on the cleaned FTO glass and dried at room temperature.

1.3 Fabrication of DSSCs

For fabrication, 0.5 mM of N719 Di-tetrabutylammonium cis-bis (isothiocyanato) bis (2, 2'-bipyridyl-4,4'-dicarboxylato)-ruthenium(II) solution was prepared with ethanol. Then the sintered TiO₂ films were dispersed into the above N719 ethanol solution at 70 °C for 12 hours. The sensitized TiO₂ films were washed with ethanol to obtain TiO₂ photoanode. The TiO₂ photoanode was placed on a light-blocking mask and clamped with the as-synthesized CEs. The open devices were obtained by injecting the liquid electrolytes into the gap between the TiO₂ photoanode and SnS-e, SnS-m and SnS-a CEs. The photoactive area of DSSCs was measured to be 0.25 cm².

2. Materials characterizations

The crystallinity and phase formation of synthesized SnS nanoparticles were analysed with the help of (Panalytical diffractometer - XPERT3) Cu k_α radiation of 1.5 nm wavelength. XRD peaks were recorded at a scan rate of 0.04 min⁻¹ in the range 0 to 80°. The morphology of the samples was analysed using SEM (JEOL-JSM-IT200) and EDAX (JEOL-JSM- IT200). The UV-Vis Drs spectra were recorded on a Shimadzu-UV1800 and for FT-IR spectra Thermo Nicolet 380 spectrophotometer was utilized. Cyclic voltammetry (CV) was recorded in a three-electrode system in an acetonitrile solution (mixture of 10 mM LiI, 0.1 mM LiClO₄ and 1mM I₂) at a scanning rate of 50 mV/s by using a BAS100 B/W electrochemical analyzer. Pt acted as a counter electrode and the Ag/Ag⁺ acted as a reference electrode. Solar energy conversion efficiency (SECE) was measured using a solar simulator (94063A, Newport Stratford Inc.) under 1 sun illumination (100 mWcm⁻²) with a sample area of 0.25 cm².

2.1. Electrochemical measurements

The electrochemical measurements of SnS nanoparticles were carried out by using three electrode system using Ag/AgCl electrode as reference, platinum electrode as a counter and Nickel foil with a mixture of active material as working electrode respectively. The working electrode was made up of SnS material, PVDF and acetylene black with a mass ratio of 80:10:10 mixed in Glutaraldehyde solution. The slurry formed was coated on Nickel strip (2.0 x 1.0 cm) and then dried at 100 °C for 12 hours. All electrochemical measurements were carried out at room temperature using an Autolab (PGSTAT101) Metrohm, Switzerland, Electrochemical Workstation, in a 0.5 M KOH aqueous solution as electrolyte.

3. Results and Discussions

3.1 Structural analysis

XRD results of SnS-e, SnS-m and SnS-a nanoparticles are shown in Fig.1. As seen from the XRD spectrum, it is confirmed that the SnS nanoparticles are formed of single-phase polycrystalline structure and the peaks are indexed as (101), (201), (011), (111), (311), (202), (211), (212), (321), (512) and (602) planes for the angular positions at 22.48°, 26.20°, 30.60°, 31.60°, 38.8°, 45.03°, 49.1°, 50.9°, 52.7°, 56.0°, 64.3° and 66.0° respectively (JCPDS card no.39-0354). XRD pattern does not show any unwanted phase corresponding to any structure confirming the purity of the products. These entire diffraction peaks match with the peaks observed in the previous report of Masoud et. al [16].

X-ray diffraction peak gets broadened in the nanocrystals due to the intrinsic strain effect as well as due to crystallite size effect and this peak broadening normally consists of two parts instrumental broadening and physical broadening [17, 18]. This corrected instrumental broadening is given by the relation [19]

$$(\beta_D)^2 = (\beta_m)^2 - (\beta_i)^2 \quad \dots (1)$$

Where β_m is the measured broadening, β_i is the instrumental broadening and β_D is the corrected broadening. The physical broadening and instrumental broadening of the sample are measured as FWHM. Using the corrected physical broadening, the average crystallite size can be calculated with the help of the Scherrer equation given as [20]:

$$D = \frac{\kappa\lambda}{\beta \cos \theta} = \frac{0.9\lambda}{\beta \cos \theta} \quad \dots (2)$$

Where λ is the Wavelength, β is the Full width half maximum, and θ is the Bragg's angle. The dislocation density was calculated by Williamson and Smallman's relation [21]:

$$\delta = \frac{n}{D^2} = \frac{1}{D^2} \quad \dots (3)$$

Where n is equal to unity, D is the crystalline size. The microstrain in the samples was calculated using the relation [22]

$$\varepsilon = \frac{\beta \cos \theta}{4} \quad \dots (4)$$

The lattice parameters were calculated according to the relation [21]:

$$\frac{1}{d_{hkl}^2} = \frac{h^2}{a^2} + \frac{k^2}{b^2} + \frac{l^2}{c^2} \quad \dots (5)$$

Where d_{hkl} represents the interplanar spacing, hkl is the Miller indices. The X-ray density was calculated by using the relation [23]:

$$P = \frac{ZM}{a^3 N_A} \quad \dots (6)$$

Where Z represents number of atoms per unit cell, P is the Density (g/cm^3), a is the Edge length in cm, M is the Molar mass in g/mol and N_A is the Avogadro's constant

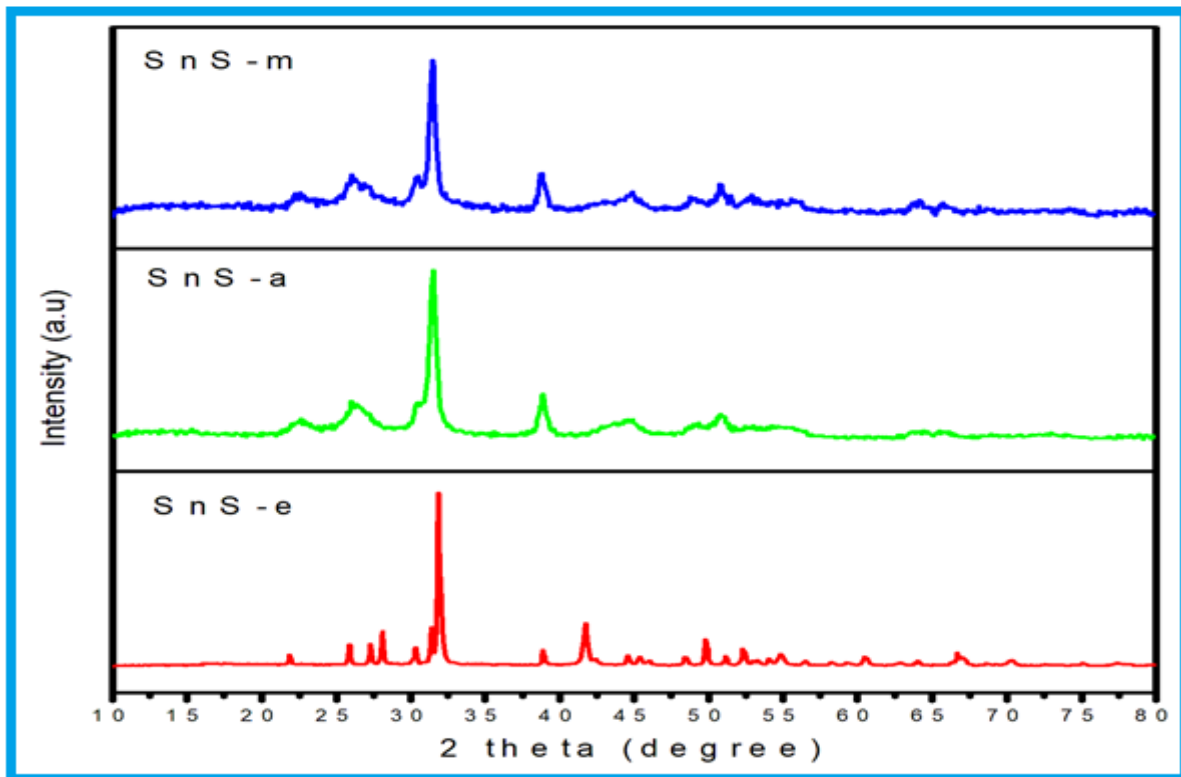


Fig.1 XRD spectra of SnS-e, SnS-a and SnS-m nanoparticles.

The calculated parameters from the XRD data are all listed in Table 1. It is observed that the crystalline size of the SnS-e, SnS-a and SnS-m nanoparticles as 28 nm, 22 nm and 19 nm respectively.

Debye Scherrer formula considers only the effect of crystalline size on the XRD peak broadening, but it doesn't tell us about the intrinsic strain, which gets developed in the nanocrystals due to the grain boundary, point defect, stacking faults and triple junction [24, 25]. To consider the effect of intrinsic strain, there are many methods such as Warren-Averbach method, Williamsons Hall method which consider the effect of this intrinsic strain and can be used for the calculation of the intrinsic strain along with the crystallite size. Above all these methods, W-H method is a very easy and simplified one [26, 27]. According to W-H method, physical line broadening of x-ray diffraction peak occurs due to the size, microstrain of the nanocrystals and the total broadening can be written as:

$$\beta_{\text{total}} = \beta_{\text{size}} + \beta_{\text{strain}} \quad \dots (7)$$

The intrinsic strain β_{strain} affects the physical broadening of the XRD profile and thus the strain-induced peak broadening can be expressed as [28]:

$$\beta_{\text{strain}} = 4\varepsilon \cdot \tan\theta \quad \dots (8)$$

So, the total broadening due to size and strain in a particular peak having the [hkl] value, can be expressed as:

$$\beta_{[\text{hkl}]} = \beta_{\text{size}} + \beta_{\text{strain}} \quad \dots (9)$$

$$\text{Where } \beta_{\text{size}} = \frac{K\lambda}{D \cos\theta} \quad \dots (10)$$

Now equation (13) can be written as:

$$\beta_{\text{hkl}} = \frac{K\lambda}{D \cos\theta} + 4\varepsilon \cdot \tan\theta \quad \dots (11)$$

Where β_{hkl} is the full width at half maximum peak intensity at different diffraction planes. On re-arranging equation (11) we can write:

$$\beta_{\text{hkl}} \cos\theta = \frac{K\lambda}{D} + 4\varepsilon \cdot \sin\theta \quad \dots (12)$$

Equation (12) is an equation of a straight line and is known as the uniform deformation model (UDM) equation, which considers the isotropic nature of the crystals. Fig.2 shows the plotting of this equation (12), with $4\varepsilon \sin\theta$ along x-axis and $\beta_{\text{hkl}} \cdot \cos\theta$ along with y-axis corresponding to each diffraction peak of SnS-e, SnS-a and SnS-m nanoparticles. The slope of this straight line provides the value of the intrinsic strain, whereas the intercept gives the crystallite size of the SnS nanocrystals. The origin of the lattice strain is attributed mainly to the lattice contraction or lattice expansion in the nanocrystals due to size confinement, because the atomic arrangement gets slightly

modified due to size confinement, compared to their bulk counterpart. On the other hand, many defects also get created at the lattice structure due to the size confinement and this in turn results in the lattice strain. The crystallite sizes have been determined from the uniform deformation model (UDM) are as 53 nm, 29 nm and 20 nm whereas the intrinsic strains are 1.1×10^{-3} , 2.5×10^{-3} and 2.2×10^{-3} .

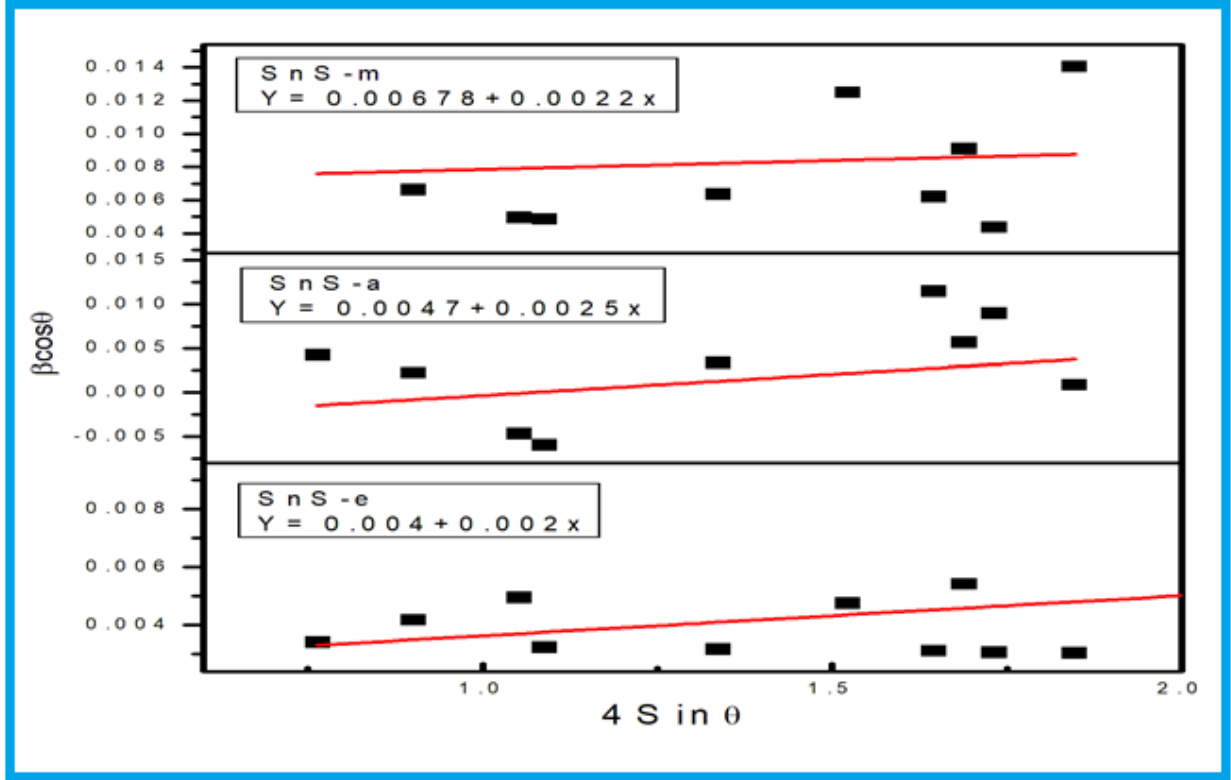


Fig 2 UDM plot of SnS-e, SnS-a and SnS-m nanoparticles.

Table.1 Structural parameters of SnS-e, SnS-a and SnS-m nanoparticles.

Samples	Crystalline size D (nm)	Microstrain $\times 10^{-3}$	W-H method		Dislocation density $\times 10^{15}$ (lines/m ²)	Lattice parameters			Volume $V = a^3$	Density g/cm ³
			D(nm)	$\epsilon \times 10^{-3}$		a	b	C		
SnS-e	28	1.5	34	2.0	2.0	11.20	3.98	4.31	192	5.21
SnS-a	22	2.1	29	2.5	5.3	11.13	3.94	4.27	188	5.34
SnS-m	19	2.1	20	2.2	5.1	10.92	3.96	4.30	186	5.38

3.2 Raman analysis

Raman spectroscopy is one of the advanced techniques to examine the chemical states and compositions of nanoparticles. Fig. 3 shows the Raman spectrum of the SnS-e nanoparticles recorded at room temperature and it clearly observed three Raman peaks at 137 cm⁻¹, 192 cm⁻¹ and 278 cm⁻¹. The lattice vibration at 137 cm⁻¹ corresponds to the B_{2u} mode, the small peak at 192 cm⁻¹ is assigned to the A_g modes and the major high intensity peak at 278 cm⁻¹ is assigned to B_{2g} mode of SnS, respectively [29].

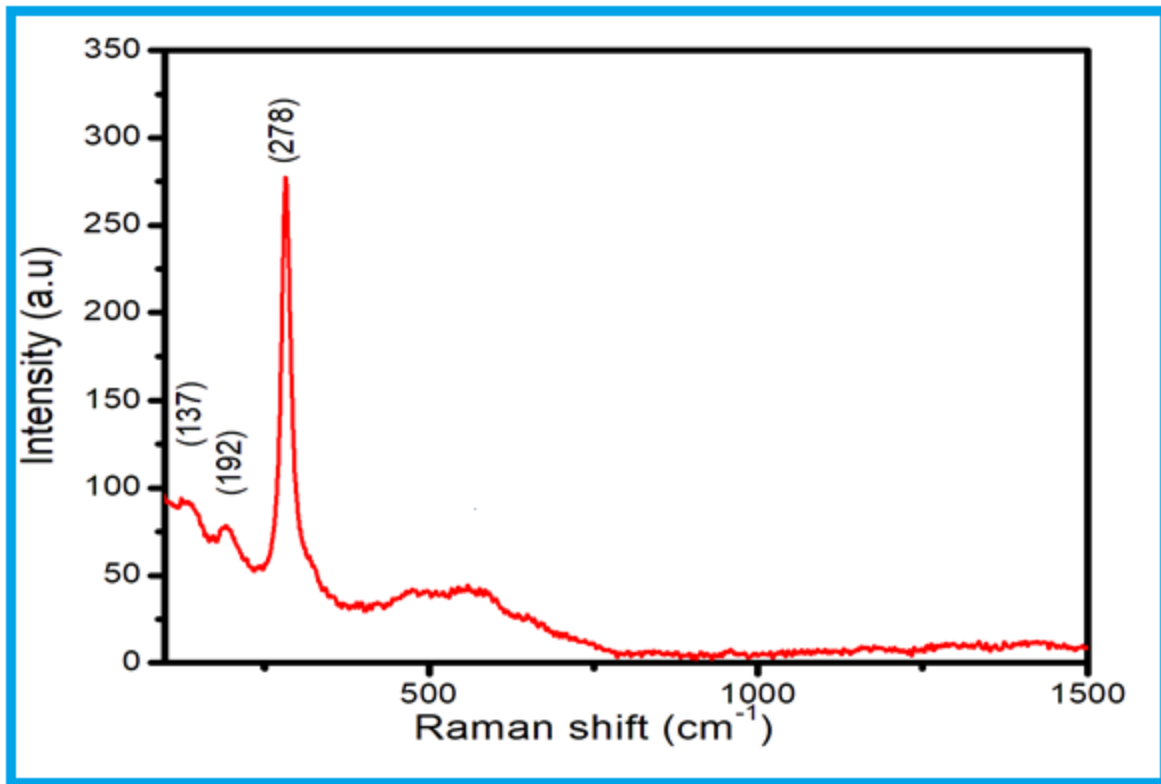


Fig.3 Raman spectrum of SnS-e nanoparticles.

3.3 Optical properties

The optical property of synthesized SnS-e nanoparticles was obtained through UV-DRs absorption spectrum (Fig. 5) within the range of 200-800 nm where the absorption peak was observed at 250 nm. The direct energy band gap values of synthesized SnS-e, SnS-a and SnS-m nanoparticles were calculated with the help of Tauc and Davis–Mott model by extrapolating the linear region of the plot with the energy axis and the intersection value corresponds to the band gap energy [30].

$$\alpha h\nu = k (h\nu - E_g)^2 \quad \dots (17)$$

Where the symbol h is Planck's constant, ν is the frequency and E_g is the energy band gap and α is the absorption coefficient and is defined by the Beer-Lambert law as follows:

$$\alpha = -\ln \frac{A}{L} \quad \dots (18)$$

Where 'A' is the absorbance and 'L' is the optical path length. Fig. 6, shows energy band gap values of the as-synthesized SnS-e, SnS-a and SnS-m nanoparticles and it is observed that the energy band gap values are 1.1 eV, 1.7 eV and 1.9 eV. The increase in direct band gap of our prepared SnS-a and SnS-m nanoparticles compared to the bulk SnS (1-1.3 eV) are due to the quantum confinement effect in the nano regime which arose from the small size of the particles as well as their morphologies [30]. Furthermore, the obtained band gap of the SnS-e nanoparticles falls in the range of optimum band gap for photovoltaic and supercapacitor applications.

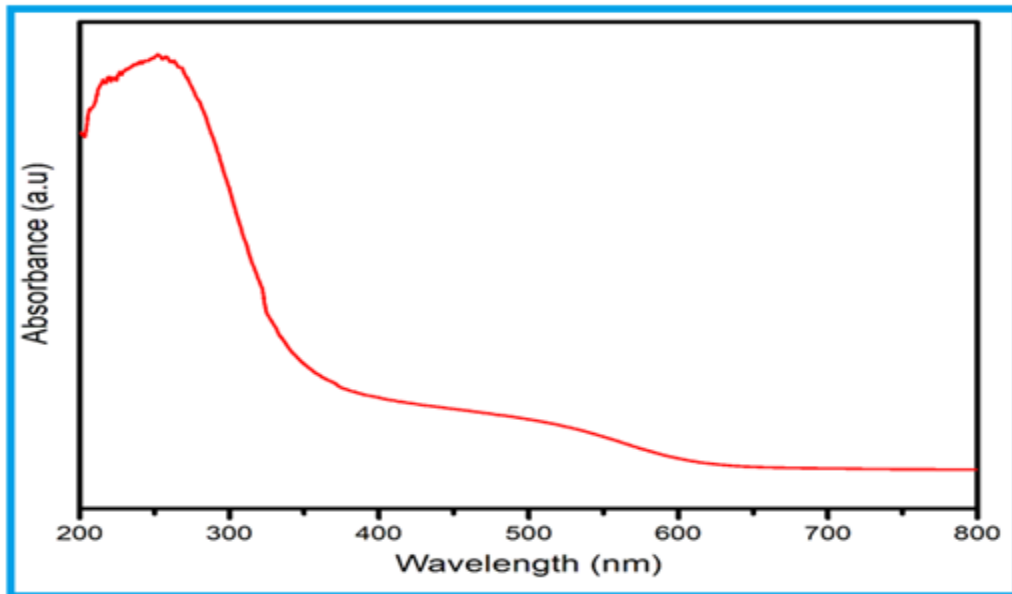


Fig 5 UV-Vis spectrum of SnS-e nanoparticles.

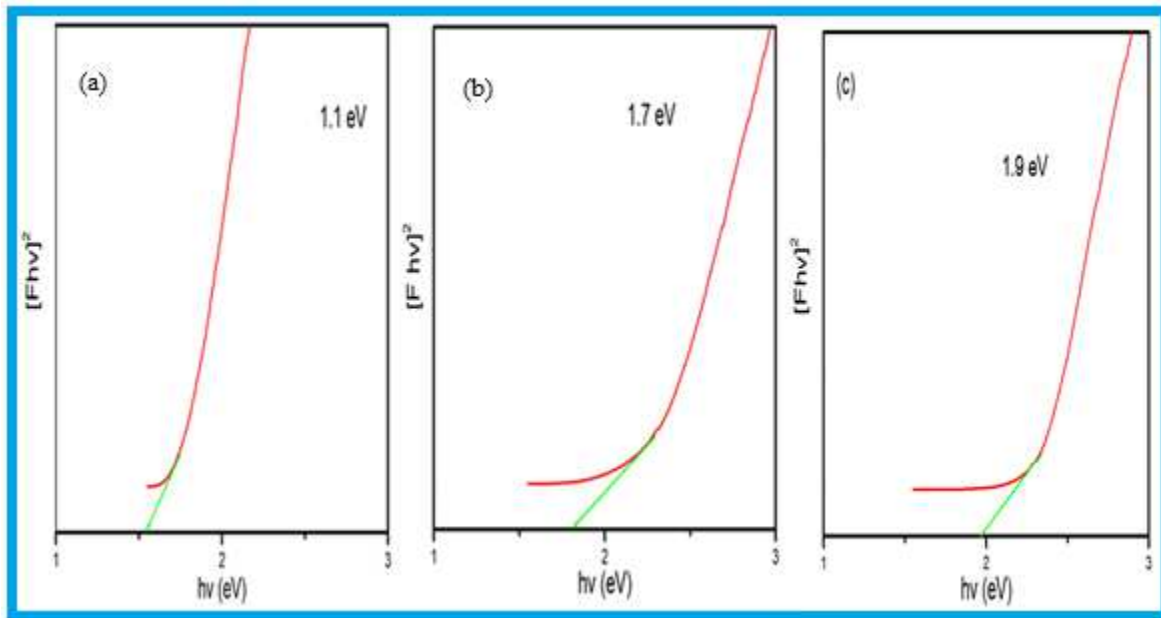


Fig. 6 direct band gap of SnS-e, SnS-a and SnS-m nanoparticles.

3.4 FT-IR analysis

FT-IR spectra of SnS-e, SnS-a and SnS-m nanoparticles are shown in Fig 6. It is observed that the spectrum of SnS-e, SnS-a and SnS-m nanoparticles shows the characteristic absorption peaks of different functional groups. The IR peaks observed in SnS-e, SnS-a and SnS-m nanoparticles are 469 cm^{-1} , 616 cm^{-1} , 620 cm^{-1} , 873 cm^{-1} , 1024 cm^{-1} , 1027 cm^{-1} , 1110 cm^{-1} , 1113 cm^{-1} , 1227 cm^{-1} , 1271 cm^{-1} , 1382 cm^{-1} , 1633 cm^{-1} , 2852 cm^{-1} , 2921 cm^{-1} , 3423 cm^{-1} and 3432 cm^{-1} , respectively. The peaks observed at 469 cm^{-1} , 616 cm^{-1} , 620 cm^{-1} , 873 cm^{-1} are attributed to disulfide stretching vibrations [31]. The peaks observed in between $1000 - 1800\text{ cm}^{-1}$ are attributed to C–O, C=C, and C=O functional groups [32], the peaks 2852 cm^{-1} , 2921 cm^{-1} corresponds to C-H stretching of an aldehyde and the peaks at 3423 cm^{-1} , 3432 cm^{-1} corresponds to the (O–H) stretch of the hydroxyl group of various functional groups, such as aldehydes, alcohols, acids, etc. The main peaks which are common in SnS-e, SnS-a and SnS-m nanoparticles are 1382 cm^{-1} , 1633 cm^{-1} , 2852 cm^{-1} , 2921 cm^{-1} represents characteristics peaks of SnS nanoparticles [33].

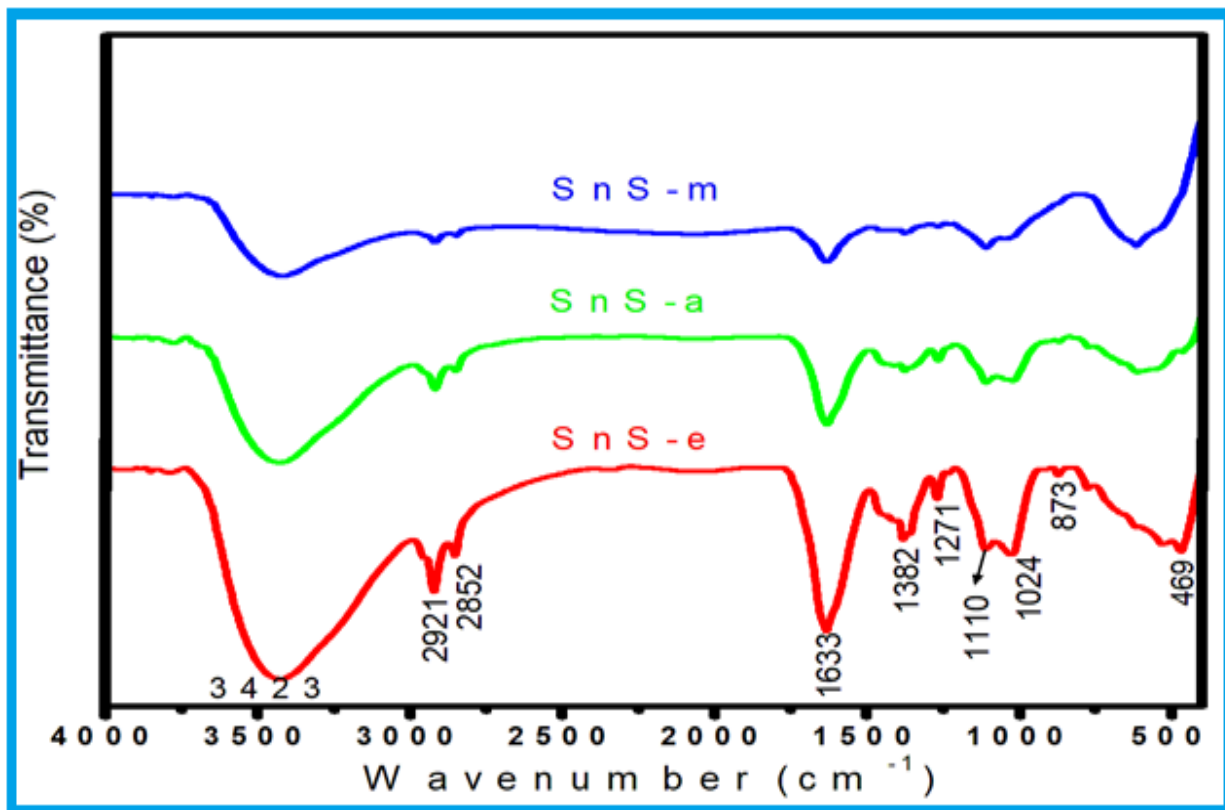


Fig.6 FT-IR spectrum of SnS-e, SnS-a and SnS-m nanoparticles.

3.5 Morphological analysis

Fig. 7 (a-f) represents the SEM images of SnS-e, SnS-a and SnS-m nanoparticles. From these SEM images, it is clear that the effect of solvents and precursors play a significant role in the morphology of SnS nanomaterials. Fig. 7a and b shows the clear spherical shapes of SnS-e nanoparticles in micrometre as well as in nanometre range. The SnS-a (Fig. 7c and d) and SnS-m (Fig.7e and f) morphology also appeared as spheres which are small in size and agglomerated may be due to the solvent acetone and methanol used in these reactions. Thus on the basis of present study, it is observed that the solvents and precursors plays very important role in construction of architectures of spherical like images of SnS nanoparticles.

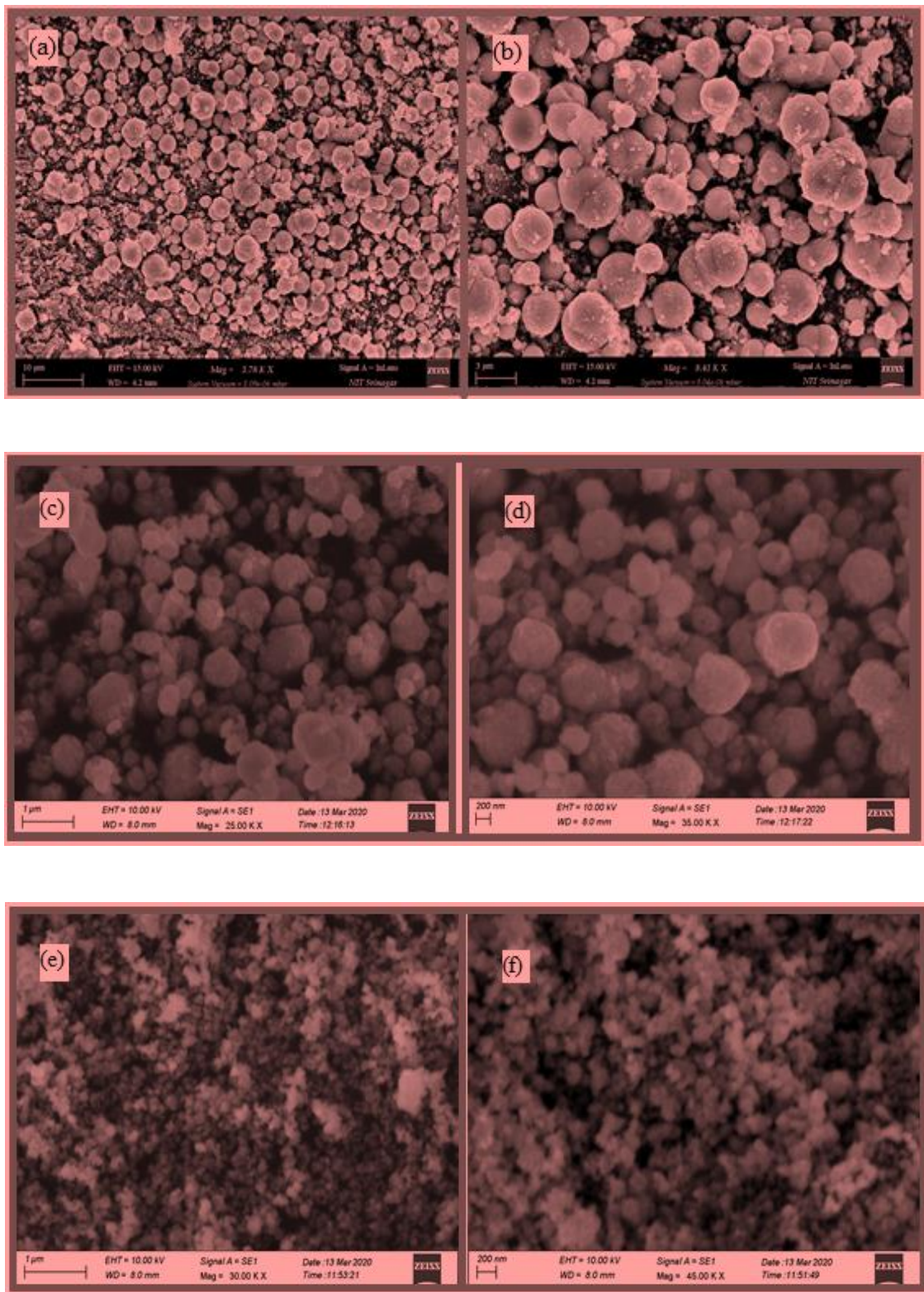
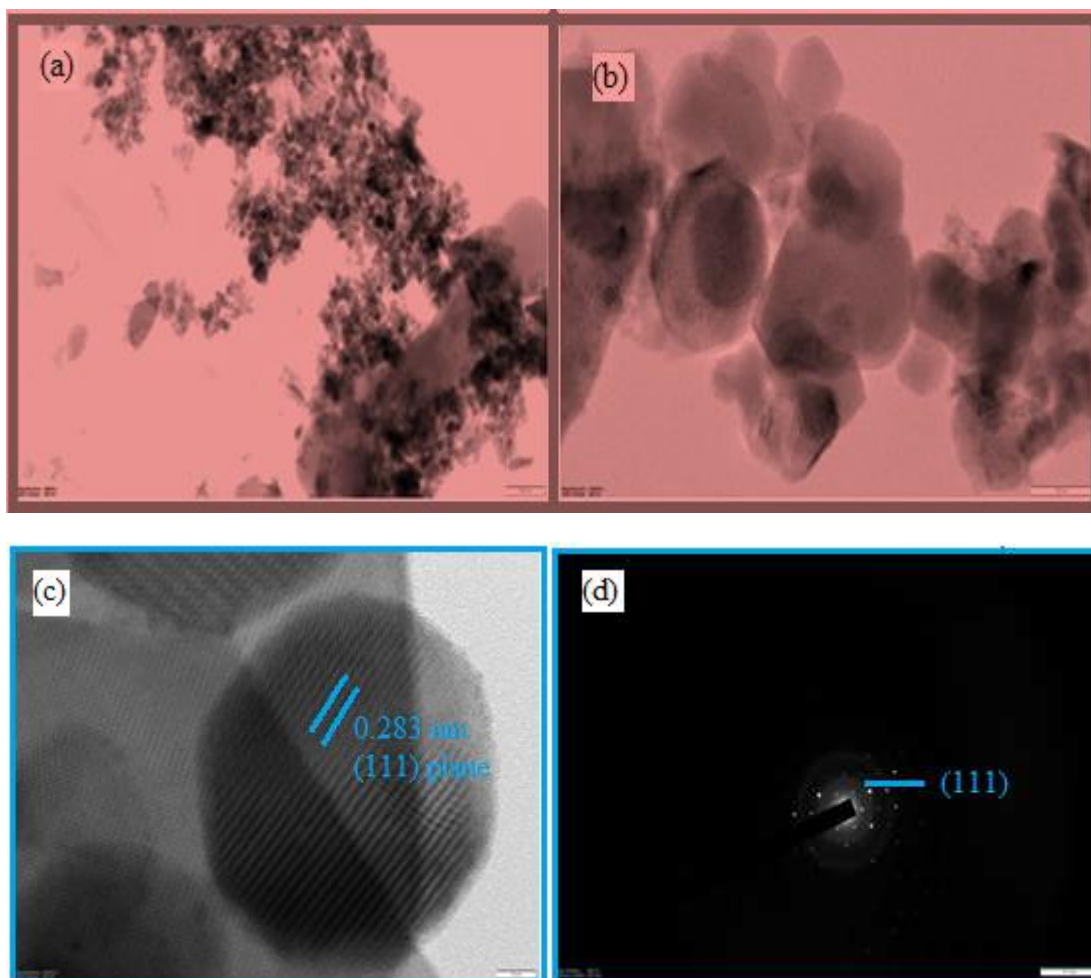


Fig. 7 (a-f) shows SEM images of SnS-e, SnS-a and SnS-m nanoparticles.

Also, TEM analysis of SnS-e nanoparticles was carried out and shown in Fig. 8 (a, b). From these TEM images, it can be seen that SnS-e nanoparticles are spherical in shape and at higher magnification of SnS-e nanoparticle (Fig.8c) shows the lattice fringes with the inter-planer spacing of 0.283 nm, which is revealed to (111) plane of orthorhombic crystal structure. The SAED pattern shows clear spot, which clearly understands polycrystalline nature of SnS-e nanoparticles (fig. 8d). From the TEM histogram (Fig.8.e), the average particle size is calculated as 29 nm and matched with the crystallite size calculated from Scherer formula (Table .1).



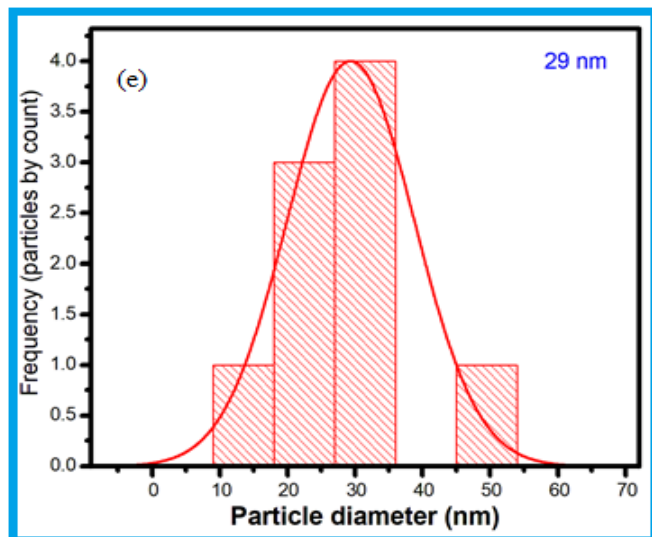


Fig. 8(a-d) shows TEM with SEAD pattern (e) Histogram of SnS-e nanoparticles

3.6 Compositional analysis

Energy-dispersive X-ray spectroscopy (EDX) investigates subjective and quantitative analysis of components that might be involved with the formation of SnS nanoparticles. Fig.8 represents the elemental composition of synthesized SnS-e nanoparticles. The EDX spectrum observes that most of the peaks are related to ‘Sn’ of mass percentage 74.49 and ‘S’ of mass percentage of 25.51 that confirms the formation and purity of SnS-e nanoparticles. The mass and atomic percentage of different elements present in the preparation of SnS-e nanoparticles are listed in table.

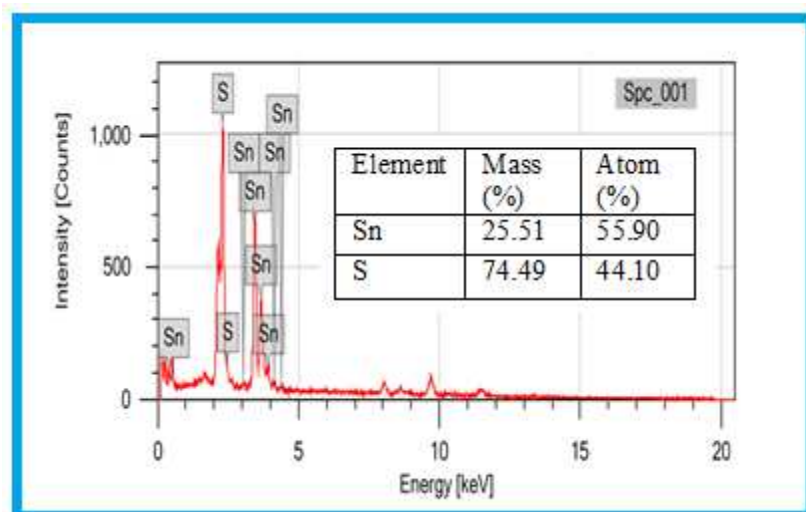


Fig. 9 EDX spectrum of SnS-e nanoparticles

3.7 Electrochemical properties

The capacitive performances of SnS-e electrode were examined by cyclic voltammetry and Galvanostatic charging/discharging techniques in 0.5 M of KOH electrolyte solution. Fig. 10 (a) represents the CV curves of SnS-e electrode at different scan rates ranging from 10 mV/s to 100 mV/s within the potential window of -1.2 to 1.5 volts. From these CV curves, the SnS-e electrode show quasi-rectangular shapes, which indicate EDLC nature of the SnS-e electrode. The area of CV curves increases from scan rate of 10 mv/s to 100 mv/s which further signifying the capacitive behavior of SnS-e electrode. From the CV curves, the specific capacitance C_s is calculated by using equation [34].

$$C_s = \frac{1}{mk(v_f - v_i)} \int_{v_i}^{v_f} I(V)dv \quad \dots (19)$$

$$C_s = \frac{S}{mk\Delta v} \quad \dots (20)$$

Where S is the area enclosed by the CV curve, m is the mass, k is the specific capacitance and Δv is the potential window. The calculated values of specific capacitance are 1581 F/g, 885 F/g, 813 F/g, 442 F/g, 405 F/g, 332 F/g, and 293 F/g for SnS-e electrode at the scan rate of 10 mV/s, 20 mV/s, 40 mV/s, 60 mV/s, 80 mV/s and 100 mV/s, respectively (fig. 10b). The observed values of specific capacitance are higher at lower scan rates as compared to higher scan rates which is due to the more time available to intercalate of OH⁻ ions at lower scan rates than that of higher scan rates [35].

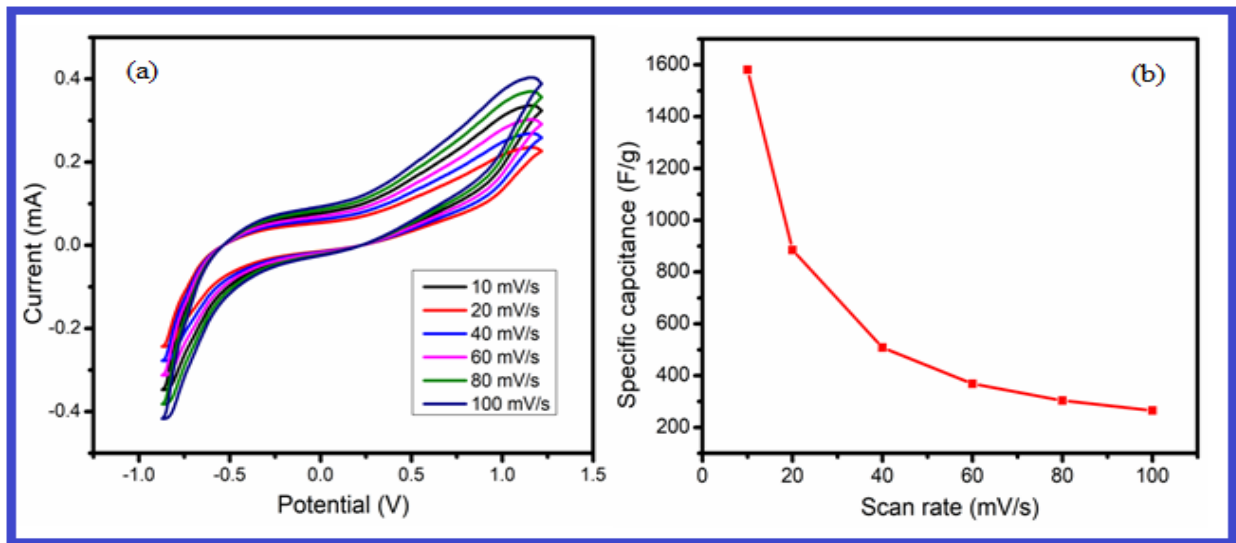


Fig. 10 (a) Cyclic voltammograms (b) Scan rate vs specific capacitance of SnS-e electrode.

The Galvanostatic charging/discharging of SnS-e electrode at a current density of 5 A/g to 10 A/g having a potential window of -0.35 to 0.35 volts in 0.5 M of KOH electrolyte is shown in Fig. 11a. The specific capacitance of SnS-e electrode can be calculated by using the following expression [36, 37]

$$C_p = \frac{I\Delta t}{m\Delta v} \quad \dots (21)$$

Where I is the current density or discharge current, Δt is the discharge time, m is the mass and Δv is the potential window. From GCD curves, the C_p values are 284F/g, 230 F/g, 221 F/g, and 215 F/g for SnS-e electrode for the current density 5 A/g, 6 A/g, 8 A/g and 10 A/g, respectively. Fig. 11b shows us the variation of specific capacitance verses current density and it is clear that the specific capacitance values decreases at higher current densities which is due to the incremental voltage drop and deficient active material being associated in the redox reaction [38].

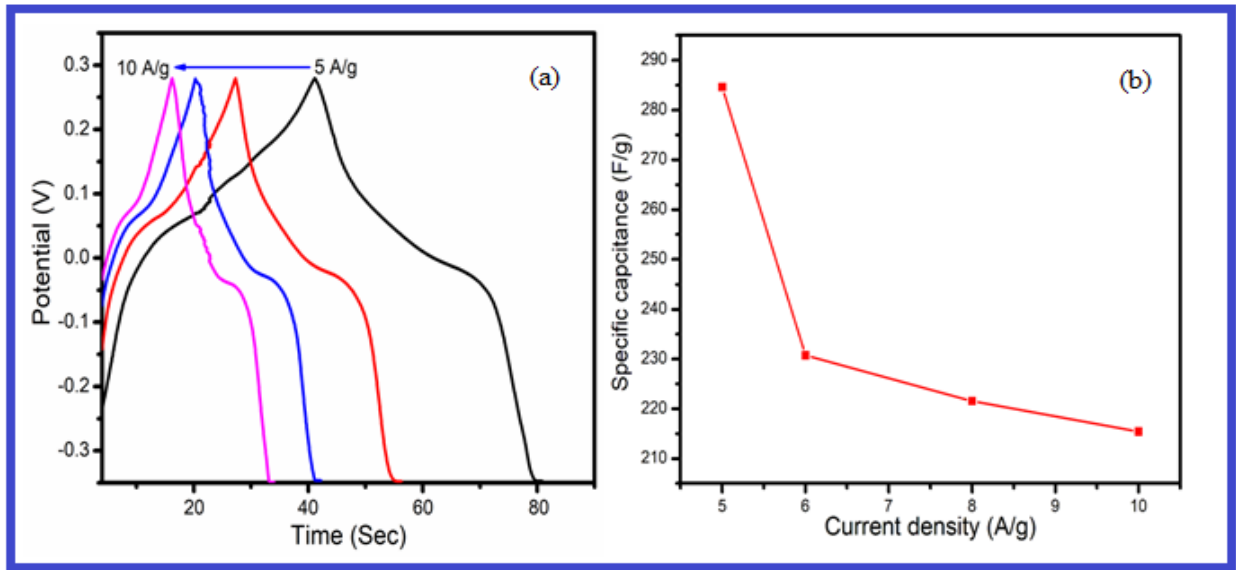


Fig. 11 (a) GCD curves SnS-e electrode. (b) Variation of current density with specific capacitance of SnS-e electrode.

The other important parameters such as energy density and powder density can be calculated by using following expressions [39].

$$E_d = \frac{1}{2}CV^2 \quad \dots (22)$$

$$P_d = \frac{E}{t} \quad \dots (23)$$

Here E_d is the energy density, C is the specific capacitance, V is the potential window, P_d is the powder density and t is the discharging time. The calculated energy densities are 216 Wh/kg, 175 Wh/kg, 168 Wh/kg and 163 Wh/kg for SnS-e. The corresponding power densities values are 1.6 KWh/kg, 1.9 KWh/kg, 2.6 KWh/kg and 3.2 KWh/kg. Fig. 12 represents the Rangone plot of SnS-e indicating SnS-e electrode exhibits the remarkable specific energy density of 216 Wh/kg with the specific power density of 1.6 KWh/kg at a current density of 5 A/g. The columbic efficiency of SnS electrode can be calculated by using the equation [39].

$$\eta = \frac{t_d}{t_c} * 100 \quad \dots (24)$$

Where η is the columbic efficiency, t_d is the discharging time and t_c is the charging time. The efficiency of SnS-e electrode is 86%.

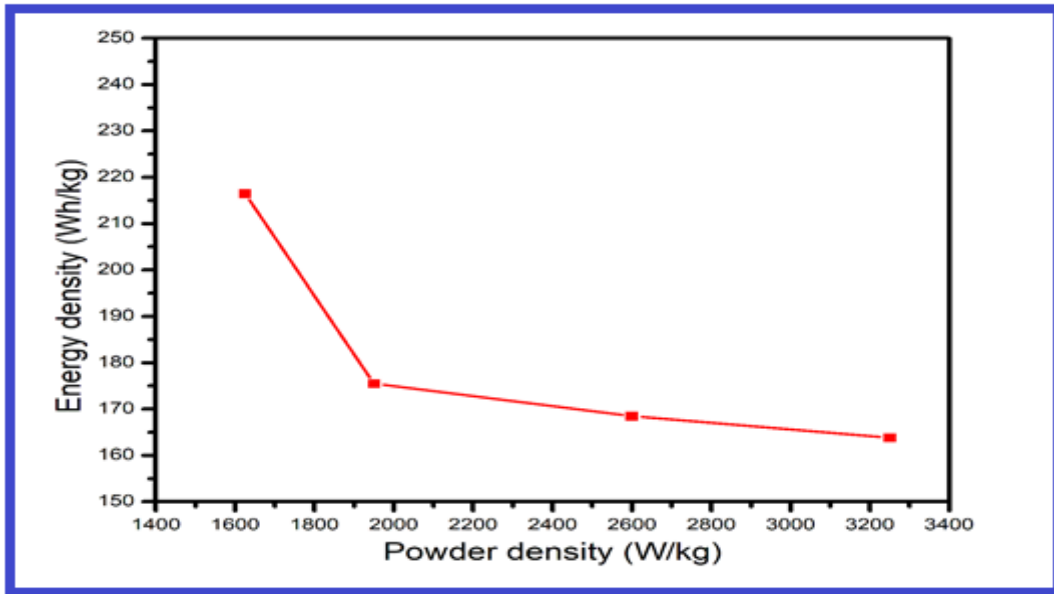
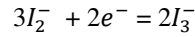
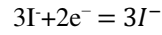


Fig. 12 Rangone plot of SnS-e electrode.

3.8 Photovoltaic performance

The photo-electrochemical measurements of SnS-e, SnS-a and SnS-m electrodes were examined in a three-electrode electro chemical workstation (CH Instruments, USA) using UV-Vis light (Xenon lamp) as a source. The CE of DSSCs was reflected by J-V curves under one sun illumination (AM 1.5 G, 100 mW cm⁻²). The electrocatalytic activity of SnS-e, SnS-a and SnS-m CEs was evaluated by CV measurement with the scanning potential varied from - 0.6 to 0.3 V at constant scan rate of 50 mV/s. The prepared electrolyte was composed of 10.0 m M LiI, 1.0 mM I₂, and 0.1 M LiClO₄ in anhydrous acetonitrile. For Tafel polarization curve measurement, asymmetrical

dummy cell was assembled based on the liquid electrolytes for the CE and measured at a scanning rate of 10 mV s⁻¹. Fig. 13a shows the cyclic voltammograms of Pt, SnS-e, SnS-a and SnS-m CEs. All these CV curves show two pairs of oxidation and reduction peaks and can be described by the equations [40]:



The relative positive pair is attributed to the oxidation and reduction of $\frac{I_2^-}{I_3^-}$ whereas the relative negative pair is attributed to the oxidation and reduction of $\frac{I^-}{I_3^-}$. The CV profile and peak positions of SnS-m, SnS-a and SnS-e and Pt CEs are similar to each other, indicating that SnS-m, SnS-a and SnS-e CEs are effective in catalyzing the reduction of tri-iodide to iodide and possess better catalytic activity.

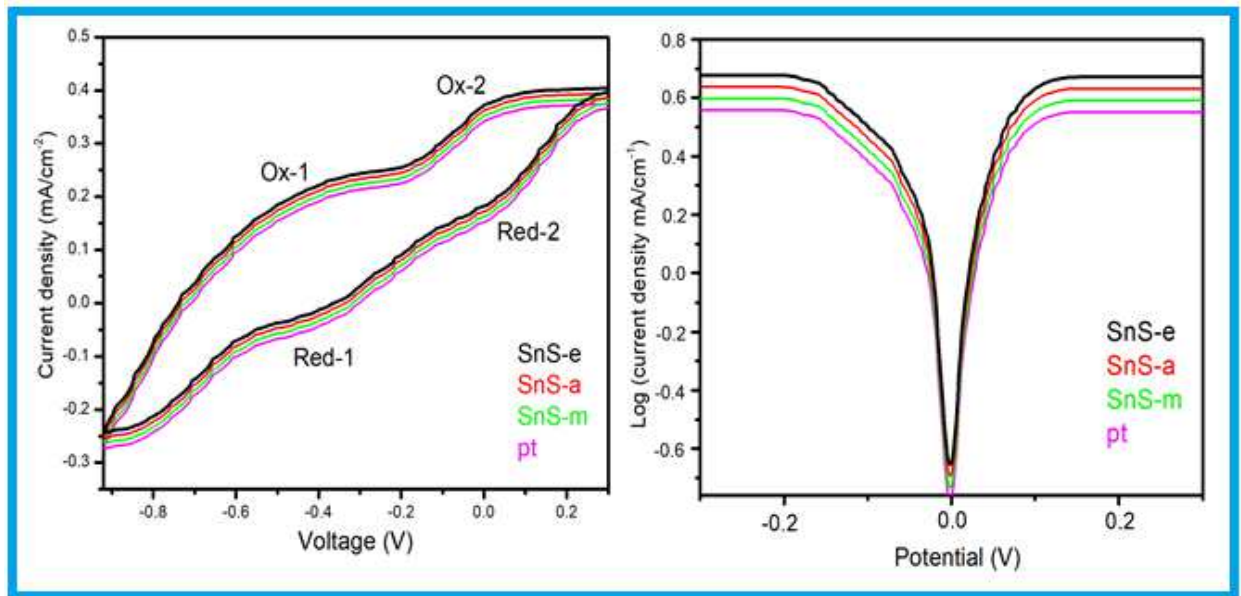


Fig. 13(a) CV curves of SnS-e, SnS-a, SnS-m and pt CEs. (b) Tafel polarization curves SnS-e, SnS-a, SnS-m and pt CEs.

Tafel polarization curves of pt, SnS-e, SnS-a and SnS-m CEs as shown in Fig. 13b. From the Fig.13b, it is clearly observed that the exchange current density and limiting diffusion current density parameters in the Tafel polarization curves has the same sequence ratios of respective electrodes. It can be seen that SnS-e electrode exhibits the strong charge transfer ability and diffusion ability than the other CEs indicating high electrocatalytic activity for the I^-/I_3^- redox couple. Thus these results are coincide with the CV results.

The effect of SnS-e, SnS-a and SnS-m CEs on the photovoltaic performance of DSSCs is systematically investigated and the resulting J-V curves are shown in Fig. 14. The obtained DSSCs Photovoltaic parameters such as open-circuit voltage (V_{oc}), short-circuit current density (J_{sc}), fill factor (FF) and photoconversion efficiency (PCE) are calculated using the following equation and the results are presented in Table 3. [41]

$$FF = \frac{I_{max}V_{max}}{I_{sc}V_{oc}} \quad \dots (25)$$

$$\eta (\%) = \frac{I_{sc}V_{oc}}{P_{in}} * FF * 100 \quad \dots (26)$$

Where ‘FF’ is the fill factor, ‘ η ’ is the photoconversion efficiency, ‘ I_{max} ’ is the maximum current density, ‘ V_{max} ’ is the maximum voltage, ‘ I_{sc} ’ is the short circuit current density, and ‘ V_{oc} ’ is the open circuit potential. The ‘ P_{in} ’ is input power in watt/cm² which is equal to $I_{max}V_{max}$.

From the J–V measurement, the I_{sc} from Pt electrode to SnS-m, SnS-a and SnS-e was observed to be 8, 8.4, 8.8 and 9.1 mAcm⁻² and the corresponding open circuit voltage ‘ V_{oc} ’ were 0.7, 0.72, 0.75 and 0.78 V, respectively. The photoconversion efficiency (η) from platinum electrode to SnS-m, SnS-a and SnS-e electrodes were 9.80 %, 9.86 %, 9.90 % and 9.99 %, respectively. From these observations, it is clear that the nanoflower-like morphology facilitates increased light absorbing ability than 1D nanostructured TiO₂ nanorods [42].

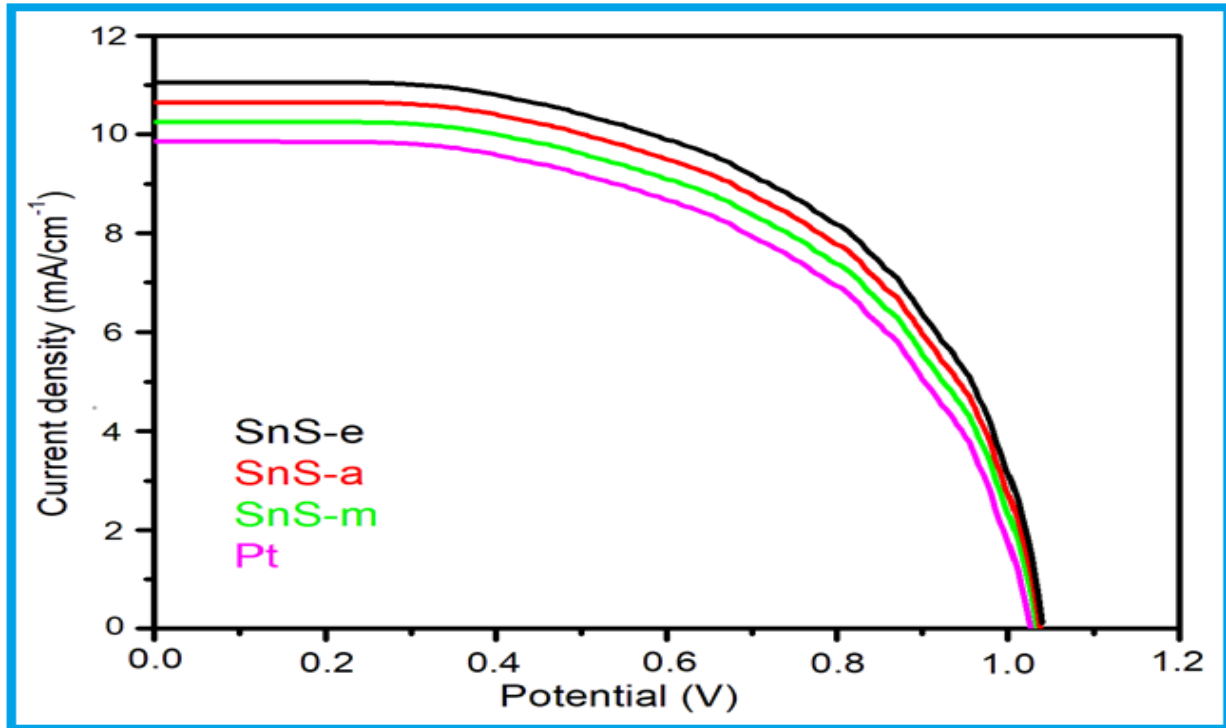


Fig.14 J–V curves of DSSCs based on SnS-e, SnS-a, SnS-m and pt CEs.

Table. 4 Photovoltaic parameters of Pt to SnS-e, SnS-a and SnS-m CEs.

CE	J_{sc} (mA cm ⁻²)	V_{oc} (V)	FF	PCE (%)
Pt	8	0.7	0.56	9.80
SnS-m	8.4	0.72	0.57	9.86
SnS-a	8.8	0.75	0.59	9.90
SnS-e	9.1	0.78	0.60	9.99

Conclusion

In this study, three different SnS nanostructures were synthesized by using cheap and easily available solvents through solvothermal method. The energy band gap of 1.1 eV is attained by nanospheres of SnS-e electrode and possesses higher specific capacitance of (1581 F/g) at the Scan rate of 10 mV/s. The DSSCs device with SnS-e nanoparticles as CEs was highest effective power conversion efficiency of 9.99 %, compared to other electrodes. Thus, this study reveals low cost method for synthesization of SnS nanoparticles in ethanol could become a promising material for supercapacitor and CEs alternative to platinum counter electrodes.

References

- [1]. A.P. Alivisatos, Science 271 (1996) 933–937.
- [2]. X. Duan, Y. Huang, R. Agarwal, C.M. Lieber, Nature 421 (2003) 241–245.
- [3]. M.S. Fuhrer, J. Nygard, L. Shih, M. Forero, Y. Young-Gui, M.S.C. Mazzoni, C.H. Joon, Science 288 (2000) 494–497.
- [4]. Z.L. Xiao, C.Y. Han, W.K. Kwok, H.H. Wang, U. Welp, J. Wang, G.W. Crabtree, J. Am. Chem. Soc. 126 (2004) 2316–2317.
- [5]. V.V. Kindyak, N.N. Koren, V.V. Moiseenko, V.F. Gremenok, Thin solid films, 207 (1992) 220-222.

- [6]. N.K.Reddy, M. Devika, E. Gopal, *Critical Reviews in Solid State and Materials Sciences*, 40 (2015) 359-398.
- [7]. S.Li, J. Zheng, Z.Hu, S.Zuo, Z.Wu, P.Yan, F.Pan, *RSC Advances*, 5 (2015) 72857-72862.
- [8].S. S. Hegde, A. G. Kunjomana, M. Prashantha, C. Kumar and K. Ramesh, *Thin Solid Films*, **545** (2013) 543–547.
- [9]. Himani Chauhan, Manoj K. Singh, S. A. Hashmi and Sasanka Deka, *RSC Adv.*, 2015, 5, 17228.
- [11]. H.L. Zhu, D. Yang, H. Zhang, *Mater. Lett.* 60 (2006) 2686–2689.
- [12]. H. Tang, J.G. Yu, X.F. Zhao, *J. Alloys Compd.* 460 (2008) 513–518.
- [13]. S. Biswas, S. Kar, S. Chaudhuri, *Appl. Surf. Sci.* 253 (2007) 9259–9266.
- [14]. C.H. An, K.B. Tang, G.Z. Shen, C.R. Wang, Q. Yang, B. Hai, Y.T. Qian, *J. Cryst. Growth* 244 (2002) 333–338.
- [15]. Qing-Song Jiang, Wenbo Li, Jing Wu, Wenjie Cheng, Jie Zhu, Zheng qing Yan, Xiaoyan Wang, Yong fen, *Journal of Materials Science: Materials in Electronics* (2019) 30:9429–9437.
- [16]. Masoud Salavati-Niasaria,b, Davood ghanbaria, Fatemeh Davar, *Journal of Alloys and Compounds* 492 (2010) 570–575.
- [17]. DebojyotiNath, Fouran Singh, Ratan Das, *Materials Chemistry and Physics* 239 (2020) 122021.
- [18].RajeswariYogamalar, Ramasamy Srinivasan, AjayanVinu, Katsuhiko Ariga, Arumugam Chandra Bose, *Solid State Communications* 149 (2009) 1919_1923.
- [19]. A. Khorsand Zak, W.H. Abd. Majid, M.E. Abrishami, RaminYousefi, *Solid State Sciences* 13 (2011) 251e256.
- [20].D. B. Cullity, 1956, *elements of X-ray diffraction*, Addison-Wesley publishing co., inc., reading Massachusetts.
- [21].G.K.Williamson and R.E.Smallman 1956, 3. *Philos. Mag.* 1(1), 34-35.
- [22]. K. M Batoor, E.H. Raslan, Y. Yang, S.F. Adil, M. Khan, A. Imran, Y Aldouri, *Aip Advances*, 9 (2019) 055202
- [23]. M. N.Ashiq, S.Irshad, M. F.Ehsanb, S.Rehmana , S. Farooq, M.Najam-Ul-Haq, A.Ziab, *New Journal of Chemistry*, Page 1 of 23, 2017.
- [24]. B.E. Warren, B.L. Averbach, *J. Appl. Phys.* 23 (4) (1952) 497.
- [25]. D. Balzar, H. Ledbetter, *J. Appl. Crystallogr.* 26 (1) (1993) 97–103.
- [26]. W.H. Hall, X-ray line broadening in metals, *Proc. Phys. Soc. Sect. A* 62 (11) (1949) 741–743.
- [27]. M.A. Tagliente, M. Massaro, *Methods Phys. Res. B.* 266 (7) (2008) 1055.
- [28]. Debojyoti Nath, Fouran Singh, RatanDas, *Materials Chemistry and Physics* 239 (2020) 122021

- [29] M. Li, Y. Wu, T. Li, Y. Chen, H. Ding, Y. Lin, N. Pan, X. Wang, *RSC Adv.* 7 (2017) 48759-48765.
- [30]. M. Parenteau and C. Carlone, *Phys. Rev. B*, 1990, 41, 5227.
- [31]. *Biopolymer Research Trends*, ed. Tamas. Nemeth, Nova Science Publishers, Inc., New York, pp-22, 29, 2008.
- [32]. C. Yohannan Panicker, H. Tresa Varghese and D. Philip, *Spectrochim. Acta, Part A*, 2006, 65, 802–804.
- [33]. L.K. Khel, S. Khan, M.I. Zaman, *Journal of chemical society of pakisthan* 27 (2005) 24-28.
- [34]. Parvin Asen, Maryam Haghighi, Saeed Shahrokhian, Nima Taghavinia, *Journal of Alloys and Compounds* 782 (2019) 38e50.
- [35]. G.S. Gund, D.P. Dubal, S.B. Jambure, S.S. Shinde, C.D. Lokhande, *J. Mater. Chem. A*, Vol. 1, pp. 4793-4803, 2013.
- [36]. A. M. Patil, A. C. Lokhande, P. A. Shinde, H. D. Shelke, C. D. Lokhande., ISSN 0974-3154 Volume 10, Number 1 (2017).
- [37]. K. Deori, S. K. Ujjain, R. K. Sharma and S. Deka, *ACS Appl. Mater. Interfaces*, 2013, 5, 10665.
- [38]. F. Beguin and E. Frackowiak, *Supercapacitors: Materials, Systems and Applications*, Wiley-VCH Verlag GmbH & Co. KGaA, 2013, ISBN 9783-527-32883-3.
- [39]. Himani Chauhan, Manoj K. Singh, S. A. Hashmi, Sasanka Deka, *RSC Adv.*, 2015, 5, 17228.
- [40]. D. Govindarajan, V. Uma Shankar, R. Gopalakrishnan, *Journal of Materials Science: Materials in Electronics*, doi.org/10.1007/s10854-019-01984-9.
- [41]. Firoz Alam, Viresh Dutta, *Applied Surface Science* xxx (2015) xxx–xxx
- [42]. Jitendra P. Sawant¹ & Rohidas B. Kale, *Journal of Solid State Electrochemistry* (2020) 24:461–472.

Figures

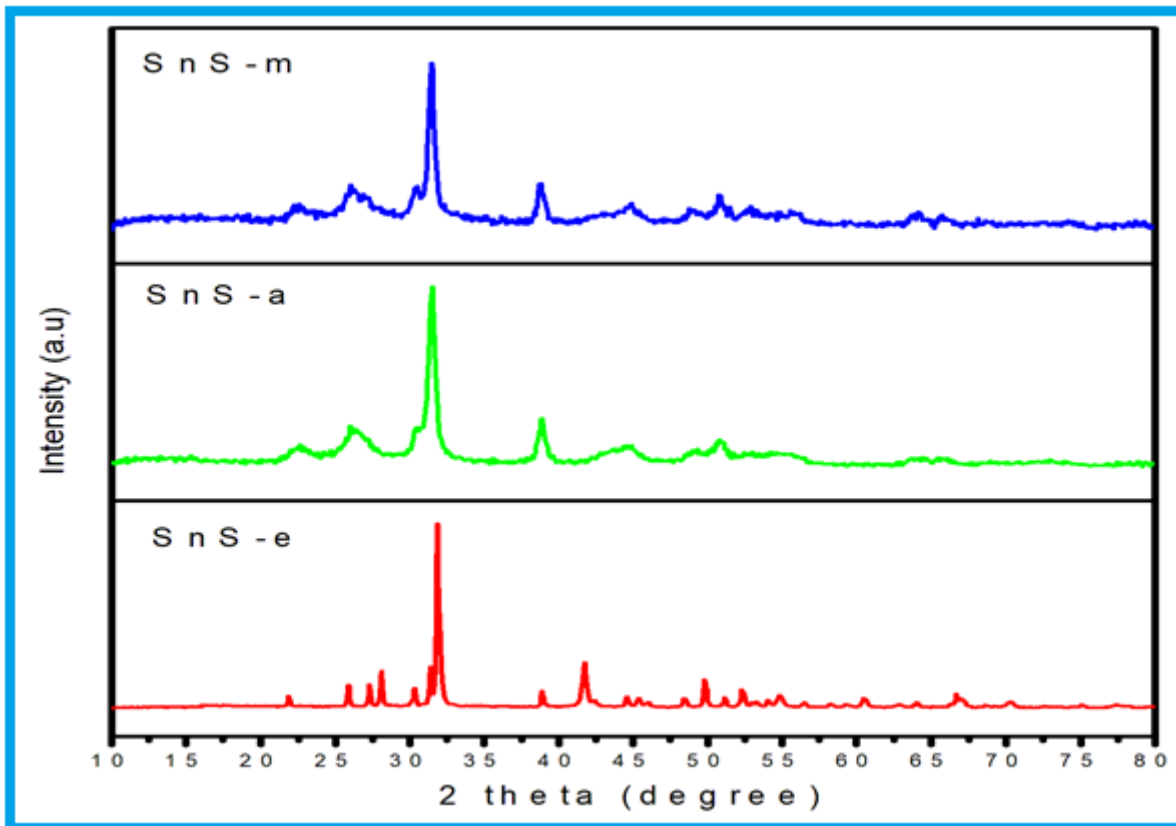


Figure 1

XRD spectra of SnS-e, SnS-a and SnS-m nanoparticles.

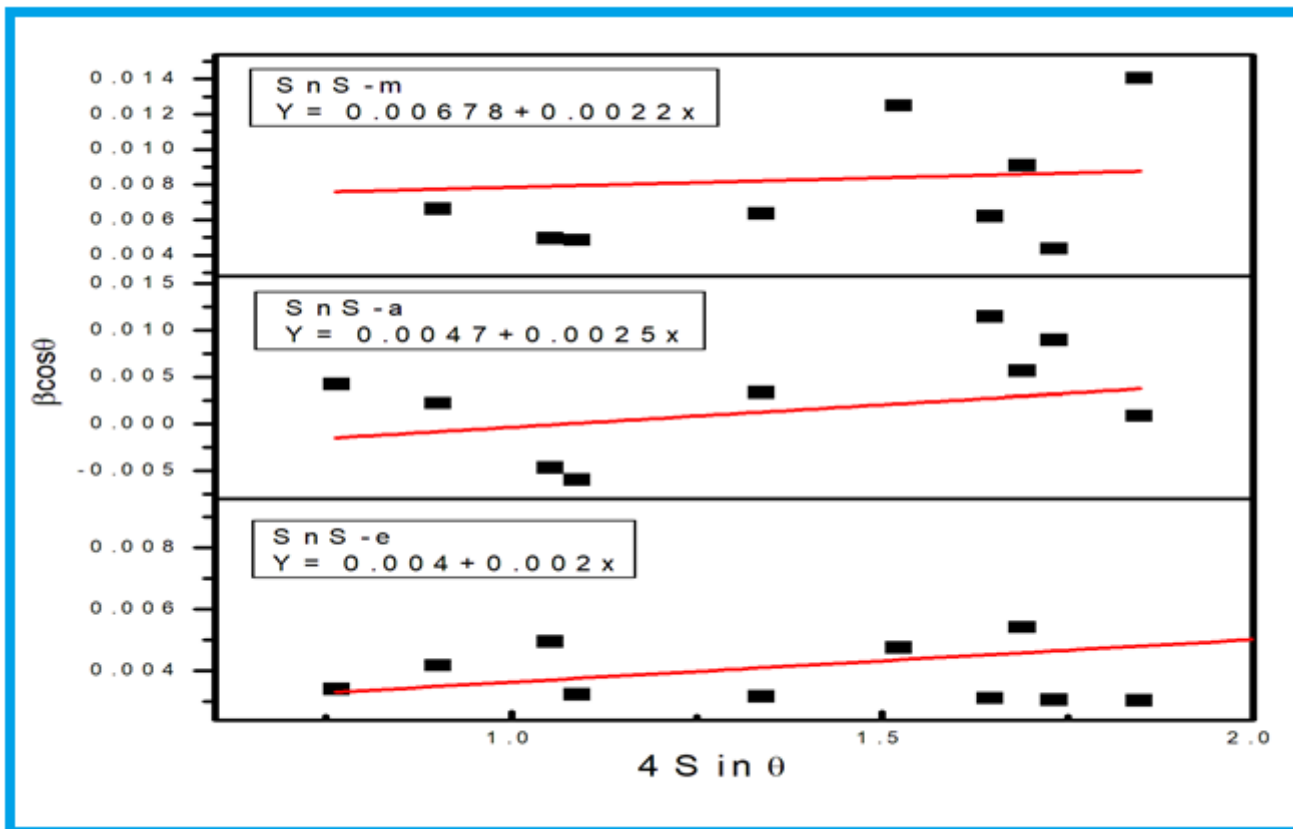


Figure 2

UDM plot of SnS-e, SnS-a and SnS-m nanoparticles.

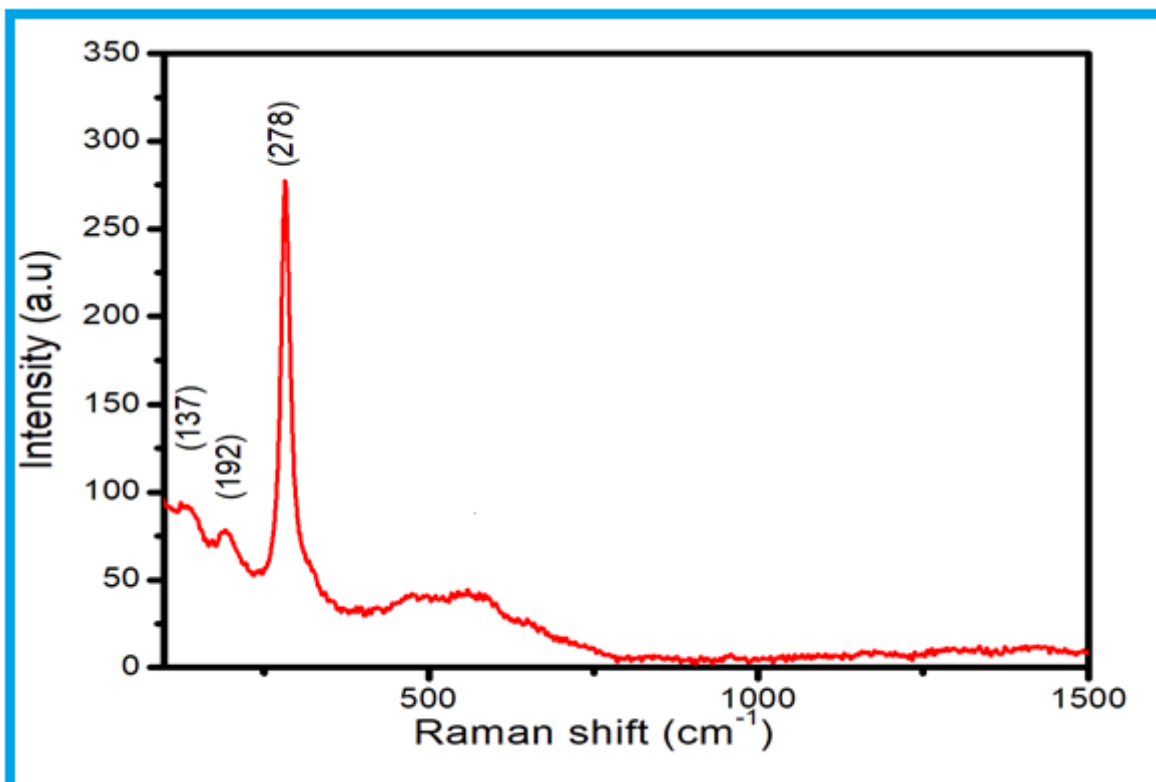


Figure 3

Raman spectrum of SnS-e nanoparticles.

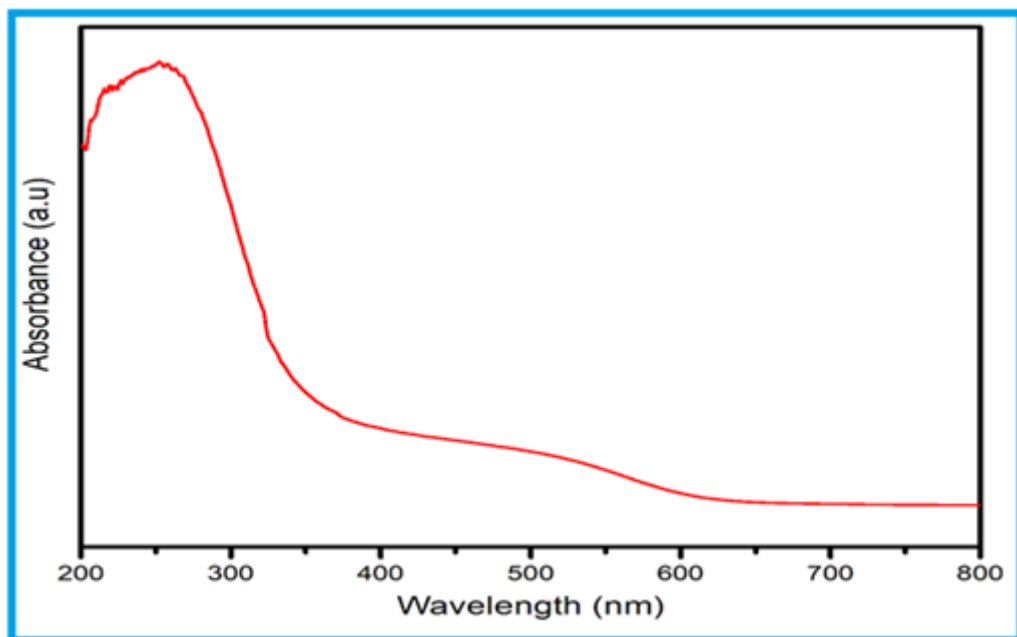


Figure 4

UV-Vis spectrum of SnS-e nanoparticles.

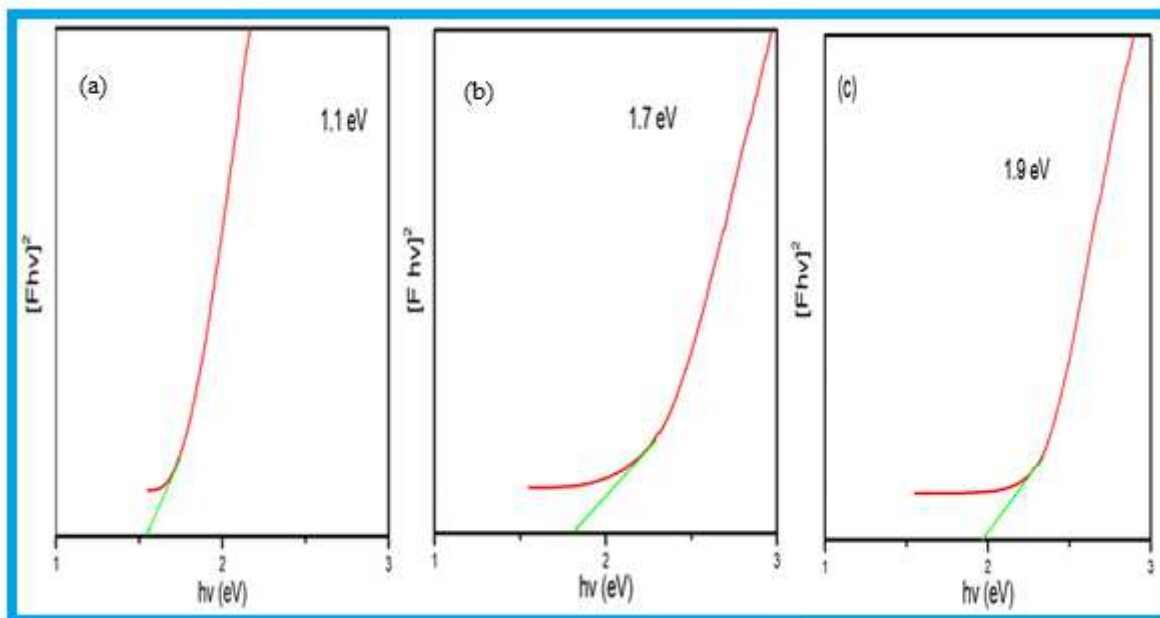


Figure 5

direct band gap of SnS-e, SnS-a and SnS-m nanoparticles.

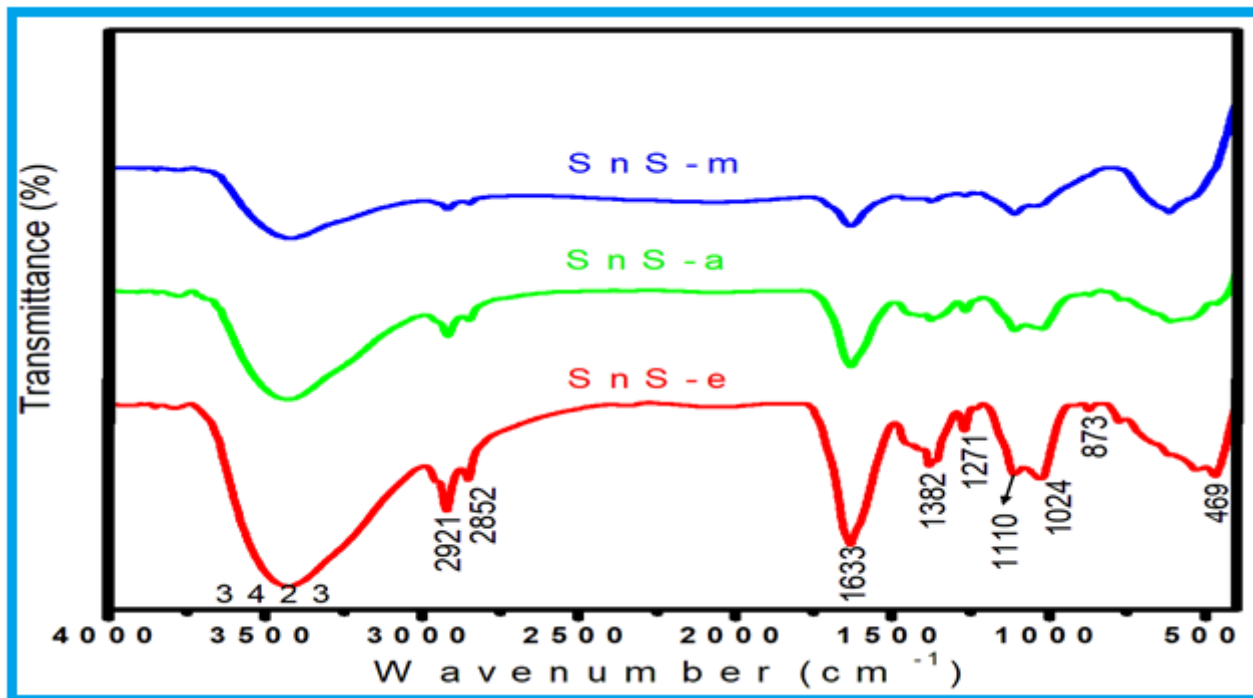


Figure 6

FT-IR spectrum of SnS-e, SnS-a and SnS-m nanoparticles.

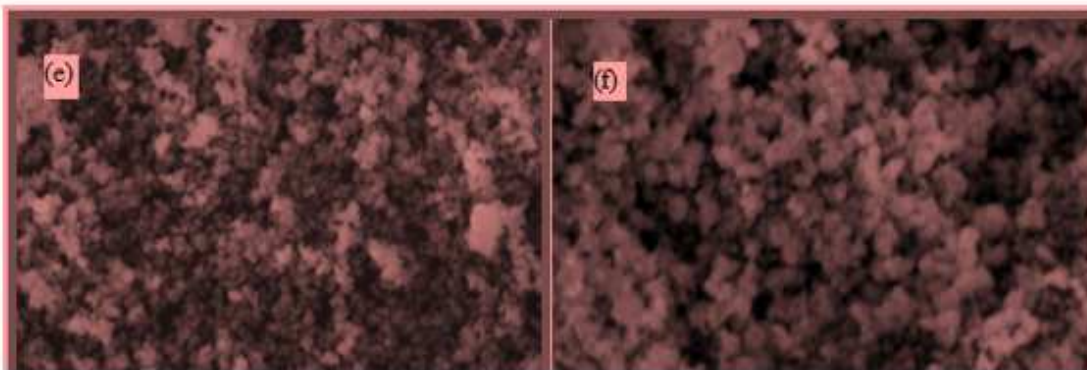
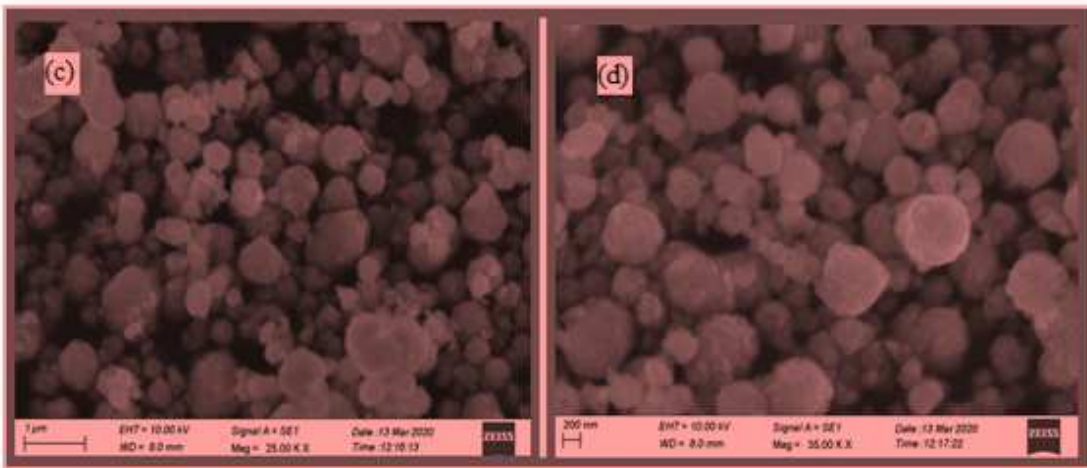
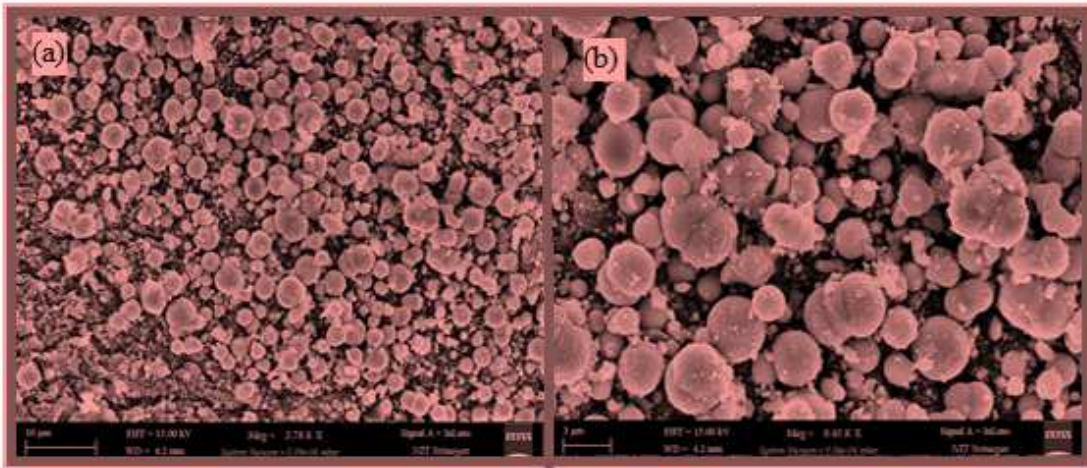


Figure 7

(a-f) shows SEM images of SnS-e, SnS-a and SnS-m nanoparticles.

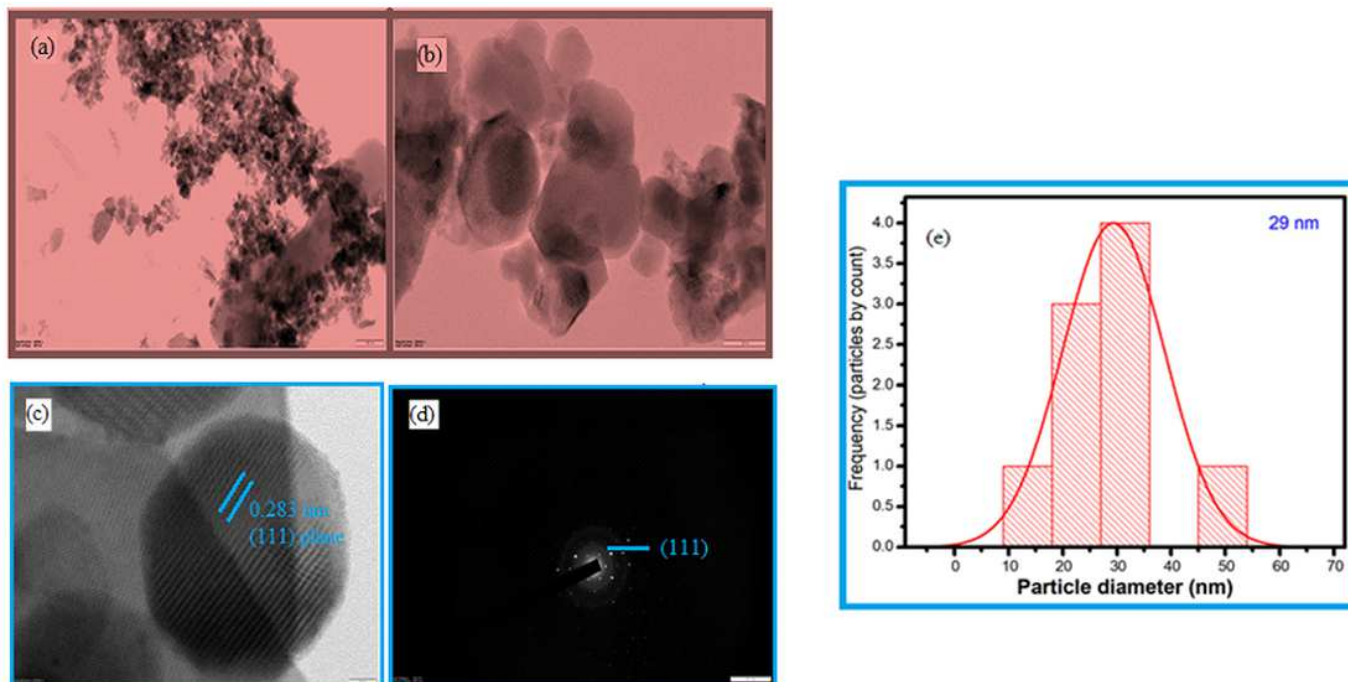


Figure 8

(a-d) shows TEM with SEAD pattern (e) Histogram of SnS-e nanoparticles

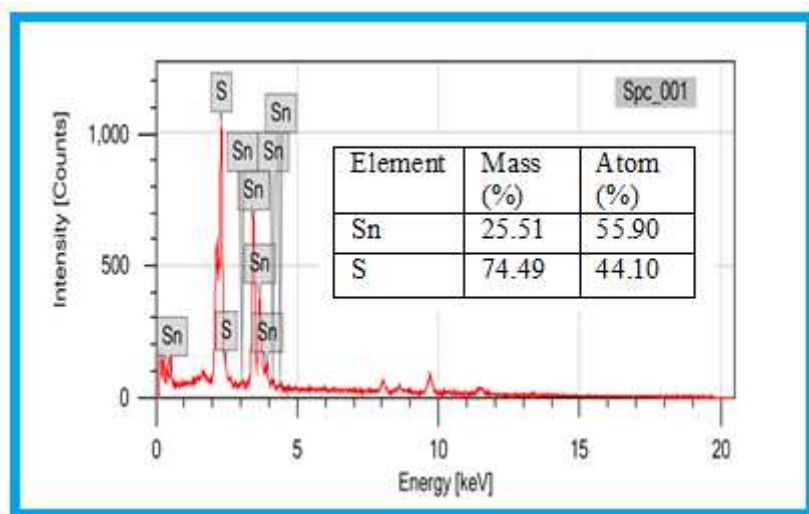


Figure 9

EDX spectrum of SnS-e nanoparticles

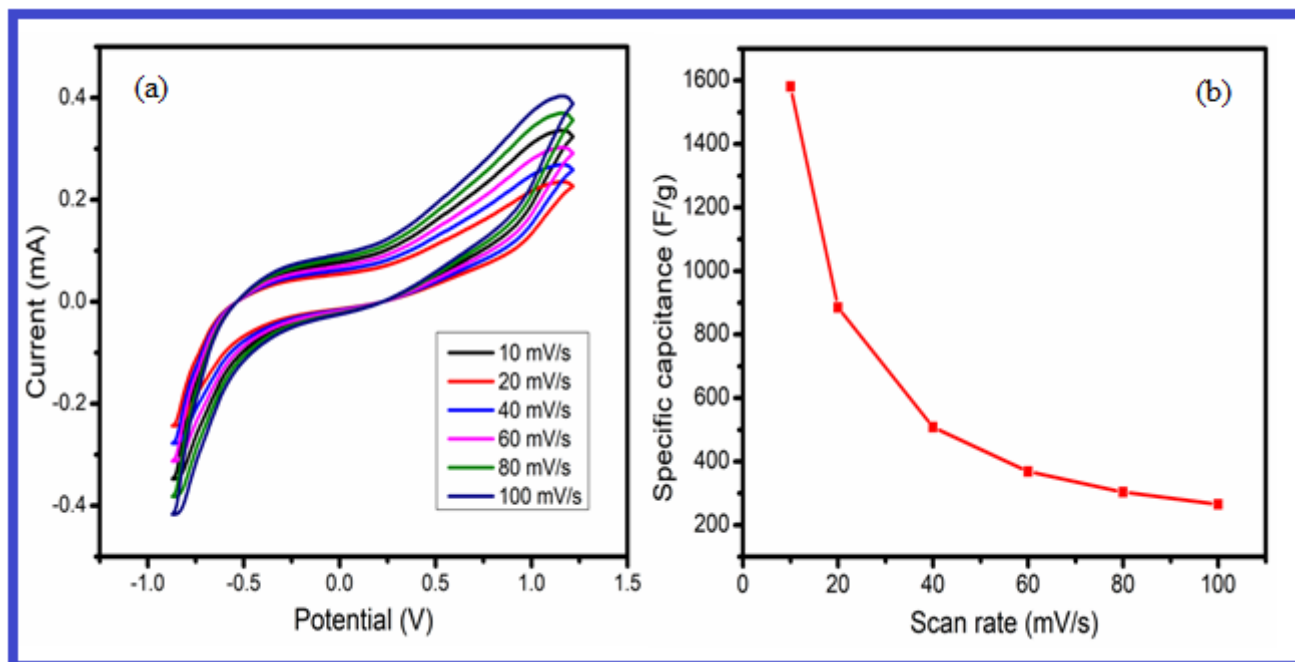


Figure 10

(a) Cyclic voltammograms (b) Scan rate vs specific capacitance of SnS-e electrode.

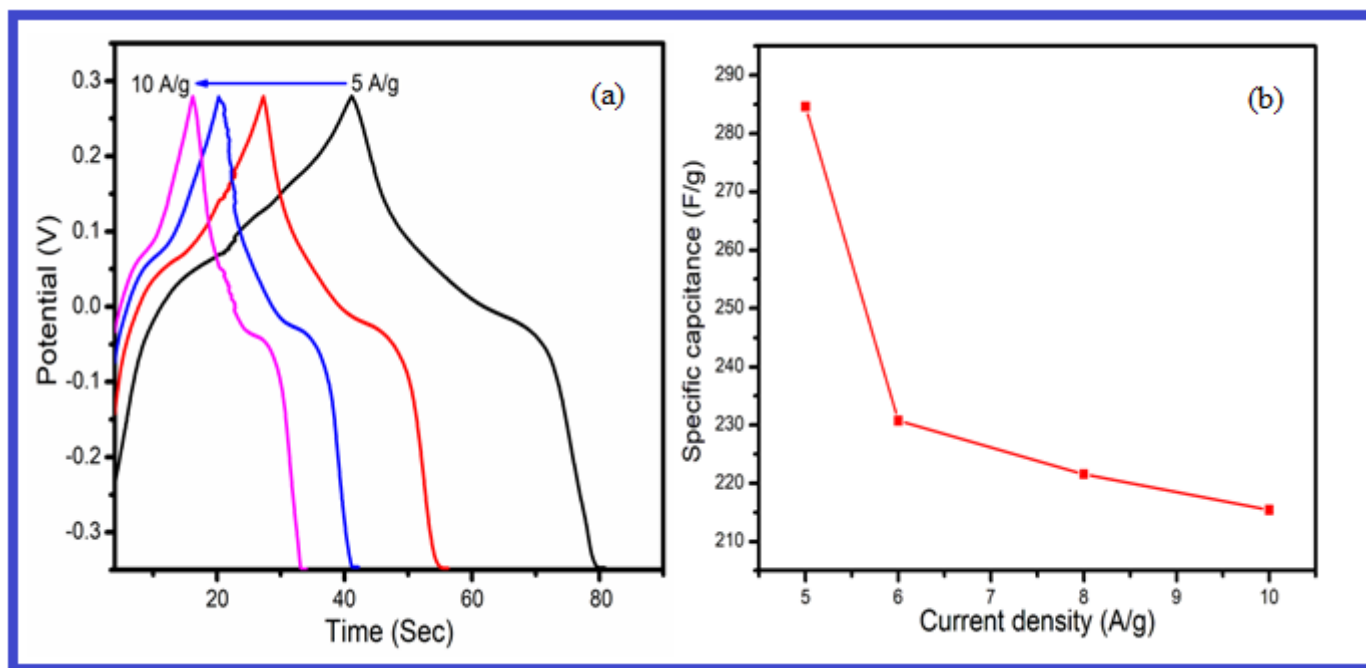


Figure 11

(a) GCD curves SnS-e electrode. (b) Variation of current density with specific capacitance of SnS-e electrode.

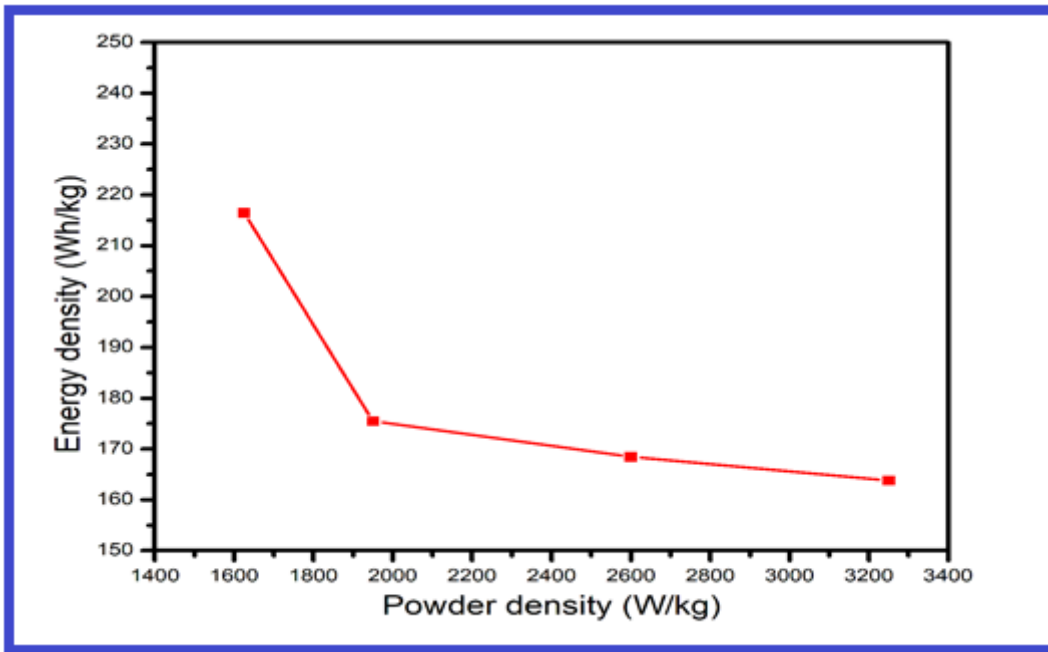


Figure 12

Rangone plot of SnS-e electrode.

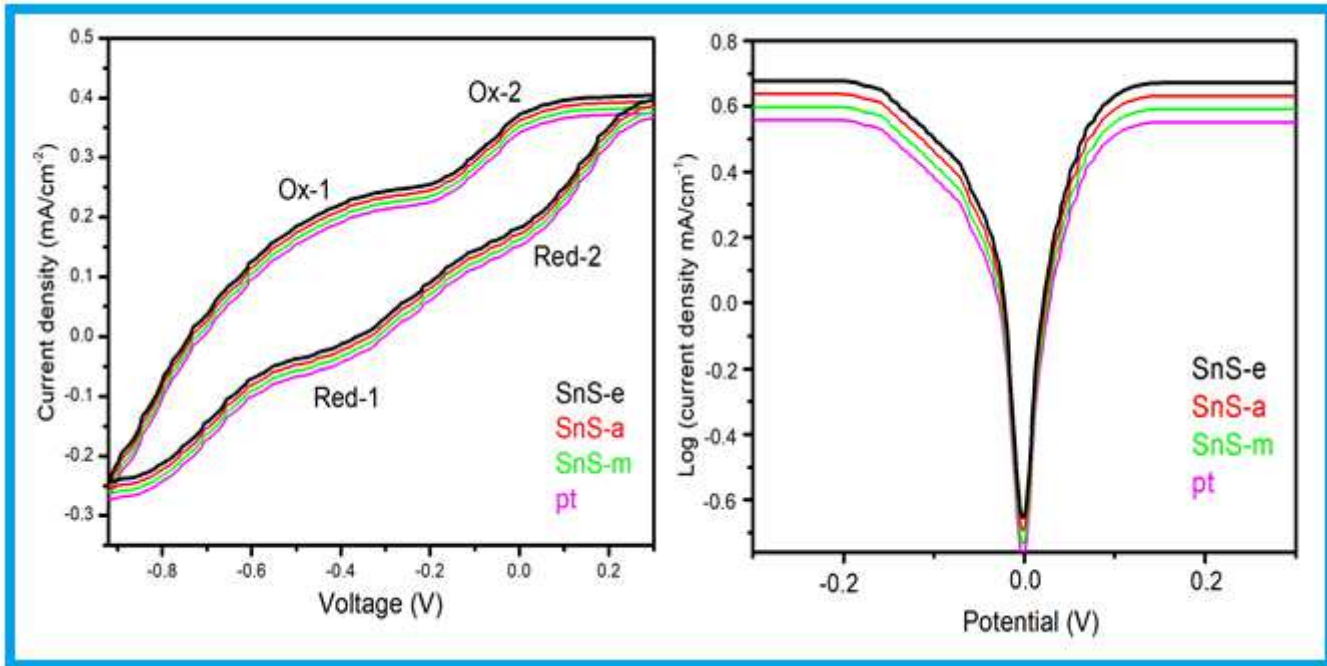


Figure 13

(a) CV curves of SnS-e, SnS-a, SnS-m and pt CE. (b) Tafel polarization curves SnS-e, SnS-a, SnS-m and pt CE.

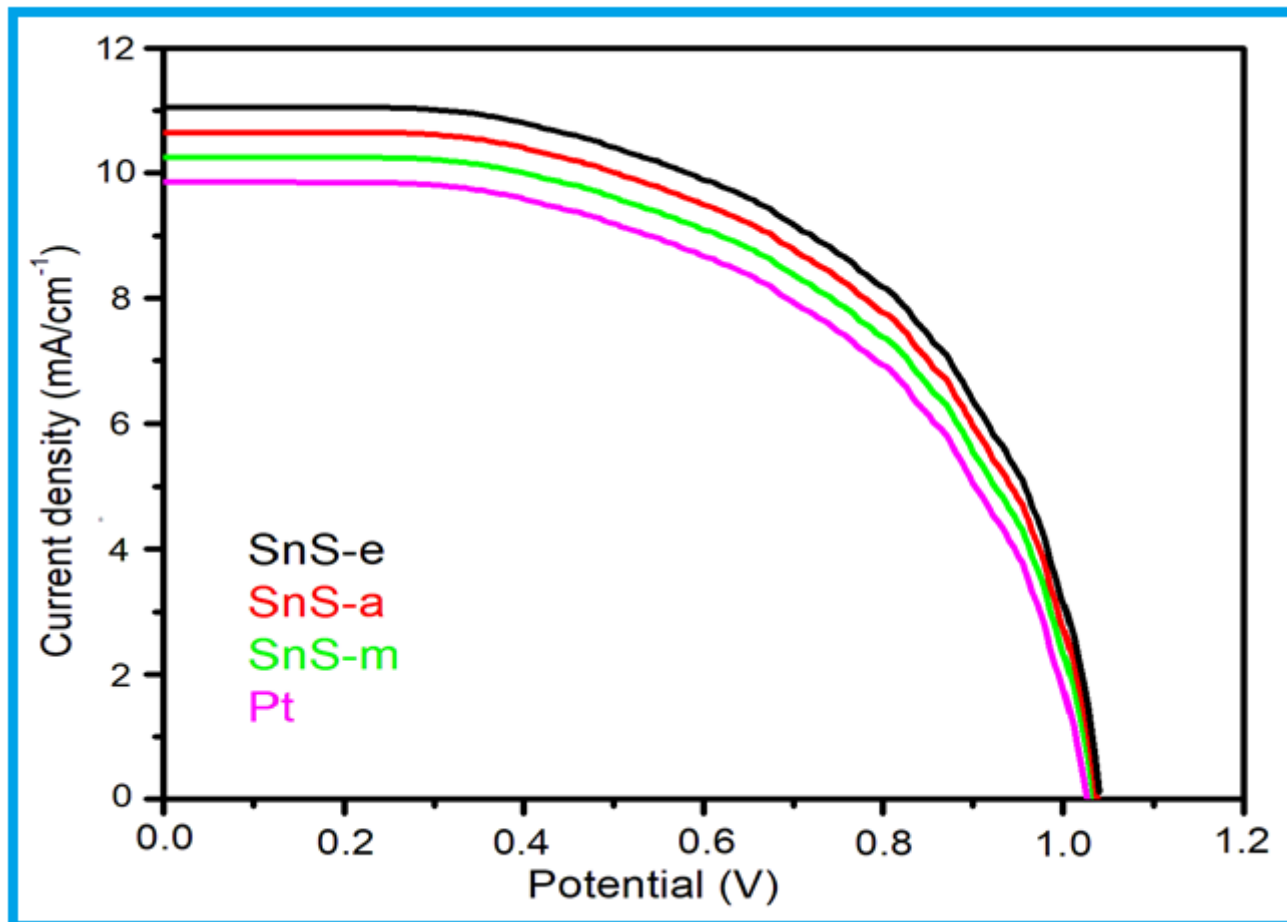


Figure 14

J-V curves of DSSCs based on SnS-e, SnS-a, SnS-m and Pt CEs.